A&A 609, A129 (2018)
DOI: 10.1051/0004-6361/201730576

Astronomy & Astrophysics

Nitrogen and hydrogen fractionation in high-mass star-forming cores from observations of HCN and HNC*

L. Colzi[1,2], F. Fontani[2], P. Caselli[3], C. Ceccarelli[4,5], P. Hily-Blant[4,5], and L. Bizzocchi[3]

[1] Università degli studi di Firenze, Dipartimento di fisica e Astronomia, via Sansone, 1 – 50019 Sesto Fiorentino, Italy
[2] INAF–Osservatorio Astrofisico di Arcetri, Largo E. Fermi 5, 50125 Florence, Italy
e-mail: colzi@arcetri.astro.it
[3] Max-Planck-Institut für extraterrestrische Physik, Giessenbachstrasse 1, 85748 Garching bei München, Germany
[4] CNRS, IPAG, 38000 Grenoble, France
[5] Univ. Grenoble Alpes, IPAG, 38000 Grenoble, France

Received 8 February 2017 / Accepted 22 October 2017

ABSTRACT

The ratio between the two stable isotopes of nitrogen, ^{14}N and ^{15}N, is well measured in the terrestrial atmosphere (~272), and for the pre-solar nebula (~441, deduced from the solar wind). Interestingly, some pristine solar system materials show enrichments in ^{15}N with respect to the pre-solar nebula value. However, it is not yet clear if and how these enrichments are linked to the past chemical history because we have only a limited number of measurements in dense star-forming regions. In this respect, dense cores, which are believed to be the precursors of clusters and also contain intermediate- and high-mass stars, are important targets because the solar system was probably born within a rich stellar cluster, and such clusters are formed in high-mass star-forming regions. The number of observations in such high-mass dense cores has remained limited so far. In this work, we show the results of IRAM-30 m observations of the $J = 1–0$ rotational transition of the molecules HCN and HNC and their ^{15}N-bearing counterparts towards 27 intermediate- and high-mass dense cores that are divided almost equally into three evolutionary categories: high-mass starless cores, high-mass protostellar objects, and ultra-compact HII regions. We have also observed the DNC(2–1) rotational transition in order to search for a relation between the isotopic ratios D/H and ^{14}N/^{15}N. We derive average ^{14}N/^{15}N ratios of 359 ± 16 in HCN and of 438 ± 21 in HNC, with a dispersion of about 150–200. We find no trend of the ^{14}N/^{15}N ratio with evolutionary stage. This result agrees with what has been found for N_2H^+ and its isotopologues in the same sources, although the ^{14}N/^{15}N ratios from N_2H^+ show a higher dispersion than in HCN/HNC, and on average, their uncertainties are larger as well. Moreover, we have found no correlation between D/H and ^{14}N/^{15}N in HNC. These findings indicate that (1) the chemical evolution does not seem to play a role in the fractionation of nitrogen, and that (2) the fractionation of hydrogen and nitrogen in these objects is not related.

Key words. radio lines: ISM – ISM: molecules – ISM: abundances

1. Introduction

Nitrogen is the fifth most abundant element in the Universe. It possesses two stable isotopes, ^{14}N and ^{15}N. Füri & Marty (2015) proposed that there are three distinct isotopic reservoirs in the solar system: the protosolar nebula (PSN), the inner solar system, and cometary ices. In the terrestrial atmosphere (TA), the typical isotopic ratio ^{14}N/^{15}N as derived from N_2 is ~272 (Marty et al. 2009). This value is almost a factor two higher than the ratio measured in nitrile-bearing molecules and in nitrogen hydrides of some comets (e.g. ~150, Manfroid et al. 2009; Shinnaka et al. 2016), and higher even by a factor five in carbonaceus chondrites (e.g. ≳50, Bonal et al. 2009). On the other hand, the ratio measured in solar wind particles collected by the Genesis spacecraft, representative of the PSN value and similar to the ratio measured on Jupiter (Owen et al. 2001), is 441 ± 6 (Marty et al. 2010). Thus, the PSN ^{14}N/^{15}N value is about twice higher than the TA value and three times higher than the value measured in comets. These measurements suggest that multiple isotopic reservoirs were present very early in the formation process of the solar system. This was recently demonstrated based on the CN/C^{15}N and HCN/HC^{15}N isotopic ratios measured in a sample of PSN analogues (Hily-Blant et al. 2017). The nature and origin of these reservoirs remain elusive, however. Currently, the two main possibilities are i) isotope-selective photodissociation of N_2 in the PSN by stellar UV (Heays et al. 2014; Guzman et al. 2017); and ii) an interstellar origin by mass fractionation reaction (Hily-Blant et al. 2013b; Roueff et al. 2015). A similar isotopic enrichment in comets, some meteorites, and interplanetary dust particles (IDPs) with respect to the PSN value has also been found for hydrogen. In the PSN, the D/H ratio is ~10^{-5} (Geiss et al. 1998), that is, similar to the cosmic elemental abundance (Linsky et al. 2006). In comets, different values of the D/H ratio were estimated: in the Jupiter-family comet 67P/Churyumov-Gerasimenko, the D/H ratio measured in H_2O is about 5×10^{-4}, approximately three times that of Earth's oceans (Altwegg et al. 2015), and other results from *Herschel* have shown D/H ~ 1.5×10^{-4} in another Jupiter-family comet, 103P/Hartley (Hartogh et al. 2011), which is same as the ratio of Earth's ocean. In carbonaceous chondrites, values of D/H ~ $1.2–2.2 \times 10^{-4}$ in hydrous silicates were obtained (Robert 2003). Furthermore, very high D/H ratios of ~10^{-2} (Remusat et al. 2009) have been found in small regions in insoluble organic matter (IOM) of meteorites and IDPs; these regions are called "hot spots". Deuterium fractionation in the interstellar medium and in solar system objects was also discussed by Ceccarelli et al. (2014).

* IRAM data used in the paper (FITS) is only available at the CDS via anonymous ftp to cdsarc.u-strasbg.fr (130.79.128.5) or via http://cdsarc.u-strasbg.fr/viz-bin/qcat?J/A+A/609/A129

From a theoretical point of view, the D/H enhancement for several species originates in a low-temperature environment where ion-molecule reactions are favoured, starting from the reaction

$$H_3^+ + HD \rightarrow H_2D^+ + H_2 + 232\ K,$$

which produces an enhanced H_2D^+/H_3^+ abundance ratio for temperatures lower than ~50 K and when H_2 is mainly in para form (e.g. Pagani et al. 1992; Gerlich et al 2002; Walmsley et al. 2004). Moreover, in dense cores, where CO freezes out onto dust grains (e.g. Caselli et al. 1999; Fontani et al. 2012), H_2D^+ can survive and H_2D^+/H_3^+ is further enhanced causing a high level of deuteration in molecules. The role of grain surface chemistry on icy material during the early cold phase is also expected to play an important role for the deuteration of neutral species such as water, formaldehyde, methanol, and complex organic molecules (e.g. Cazaux et al. 2011; Taquet et al. 2012, 2013). The reason is that the enhanced abundances of the deuterated forms of H_3^+ (H_2D^+, D_2H^+, D_3^+) produce enhanced abundances of D atoms in the gas phase upon their dissociative recombination with electrons. The enhanced D abundance implies a higher D/H ratio, so that unsaturated molecules on the surface (in particular CO) can be deuterated as well as hydrogenated to produce singly and doubly deuterated water and formaldehyde as well as singly, doubly, and triply deuterated methanol (e.g. Caselli & Ceccarelli 2012; Ceccarelli et al. 2014).

In principle, similar gas-phase mass fractionation reactions can also produce ^{15}N enrichments under cold and dense conditions. This motivated the search for correlated enrichments in D and ^{15}N in cosmomaterials (Aléon et al. 2009), although chemical models suggest that such correlations may not be present (Wirström et al. 2012). Furthermore, while the above scenario of D-enrichments through ion-neutral mass fractionation reactions has been firmly proved for D through observations of low- and high-mass star-forming regions (e.g. Crapsi et al. 2005; Caselli et al. 2008; Emprechtinger et al. 2009; Fontani et al. 2011), the reasons for ^{15}N enrichment are still highly uncertain. For example, $HC^{15}N$ and $H^{15}NC$ could be formed through the dissociative recombination of $HC^{15}NH^+$: Terzieva & Herbst (2000) found that the reaction that causes most of the N-fractionation is the exchange reaction between ^{15}N and $HCNH^+$,

$$^{15}N + HCNH^+ \rightarrow N + HC^{15}NH^+ + 35.1K,$$

but they assumed that this reaction could occur without an energy barrier. The most recent and complete chemical models (Roueff et al. 2015) are implemented with the recent discovery that this reaction has an energy barrier, and they indicate that ^{15}N should not be enriched during the evolution of a star-forming core, not even at the very early cold phases. Moreover, observational works devoted to testing these predictions are still very limited.

In the few low-mass pre-stellar cores or protostellar envelopes observed so far, values of $^{14}N/^{15}N$ comparable to the value of the PSN have been measured from N_2H^+ and NH_3 (330 ± 150 in N_2H^+, Daniel et al. 2016; 350–500, Gerin et al. 2009; 334 ± 50, Lis et al. 2010 in NH_3), or even higher (1000 ± 200 in N_2H^+, Bizzocchi et al. 2013). Conversely, through observations of the nitrile-bearing species HCN and HNC in low-mass sources, the $^{14}N/^{15}N$ ratio was found to be significantly lower (140–360, Hily-Blant et al. 2013a; 160–290, Wampfler et al. 2014). Moreover, low values have recently also been found in protoplanetary discs (from 80 up to 160, Guzmán et al. 2017), but these results are based on a low statistics (six protoplanetary discs). From the point of view of chemical models, differential fractionation is expected between nitriles and hydrides (Wirström et al. 2012; Hily-Blant et al. 2013a,b), although the most recent models (Roueff et al. 2015) do not support this scenario. However, none of these models is able to reproduce the low fractionation observed in N_2H^+ towards L1544 (Bizzocchi et al. 2013) and the large spread reported by Fontani et al. (2015a).

To investigate the possible correlation between D and ^{15}N enrichments in interstellar environments, Fontani et al. (2015a) conducted a survey of the $^{14}N/^{15}N$ and D/H isotopic ratios towards a sample of high-mass cores in different evolutionary stages and found a possible anti-correlation, which was quite faint, however, and was obtained from a low number (12 objects) of detections. In addition, no correlation between the disc-averaged D/H and $^{14}N/^{15}N$ ratios have been measured by Guzmán et al. (2017) in six protoplanetary discs, but again the conclusion is based on poor statistics. Another intriguing result is that the D- and ^{15}N-enhancements are not always observed in the same place in pristine solar system material (Busemann et al. 2006; Robert & Derenne 2006). It is therefore important to gather more data in sources that are good candidates to represent the environment in which our Sun was born to place stringent constraints on current chemical models. In this respect, intermediate- and high-mass star-forming cores are interesting targets because growing evidence shows that the Sun was born in a rich cluster that also contained massive stars (Adams 2010; Banerjee et al. 2016). Moreover, Taquet et al. (2016) have recently proposed that the proto-Sun was born in an environment that was denser and warmer than has commonly been considered for a solar system progenitor. In any case, because the statistics is still poor, more observations in star-forming cloud cores in different evolutionary stages are useful for a better understanding of whether and how the ^{15}N fractionation process might be influenced by evolution. An example of existing work about ^{15}N fractionation in high-mass dense cores is Adande & Ziurys (2012). These authors worked with a larger beam than was used in our observations, and they did not have an evolutionary classification of the sources, which makes interpreting their results in an evolutionary study difficult.

We here report the first measurements of the $^{14}N/^{15}N$ ratio derived from HCN and HNC in a sample of 27 dense cores associated with different stages of the high-mass star formation process that have previously been studied for their deuterated molecules and the ^{15}N-bearing species of N_2H^+ (Fontani et al. 2011, 2015a,b). In particular, Fontani et al. (2015a) for the first time measured the $^{14}N/^{15}N$ isotopic ratio in N_2H^+ towards the same sources. These new data therefore allow us to investigate the possible difference between nitrogen hydrides and nitrile-bearing species that have been proposed by both theoretical studies (Wirström et al. 2012) and observational findings (Hily-Blant et al. 2013a). We also report measurements of the D/H ratios for HNC to search for relations between the two isotopic ratios.

2. Observations

We performed observations of the $J = 1$–0 rotational transition of $H^{15}NC$, $HN^{13}C$, $HC^{15}N$, and $H^{13}CN$ towards the 27 sources observed by Fontani et al. (2015a) from 6 to 9 June 2015, using the 3 mm receiver of the IRAM-30 m telescope. We refer to this paper for the description of the source sample. We simultaneously observed the $J = 2$–1 transition of DNC with the 2 mm receiver. Table 1 presents the observed spectral windows and some main technical observational parameters. Table 2 presents the hyperfine frequencies of $H^{13}CN$. The atmospheric

Table 1. Line rest frequencies and observational parameters.

Line	Frequency GHz	HPBW arcsec	Δv^* km s^{-1}	T_{sys} K	η_{MB}	F_{eff}
HC^{15}N(1–0)	86.0549	28	~0.16	100–150	0.85	0.95
H^{13}CN(1–0)	86.3399	28	~0.16	100–150	0.85	0.95
HN^{13}C(1–0)	87.0908	28	~0.16	100–150	0.85	0.95
H^{15}NC(1–0)	88.8657	27	~0.16	100–150	0.84	0.95
DNC(2–1)	152.60977	15	~0.096	200–250	0.78	0.93

Notes. (*) Velocity resolution of the spectrum.

Table 2. Frequencies of the hyperfine components of the transition H^{13}CN(1–0).

J'–J''	F'–F''	Frequency (GHz)
1–0	1–1	86.33873
	2–1	86.34016
	0–1	86.34225

Notes. F is the quantum number associated with the sum between the orbital angular momentum $|J|$ and the ^{14}N nuclear angular momentum. The hyperfine spitting due to ^{13}C is negligible.

conditions were very stable during the whole observing period, with precipitable water vapour usually in the range 3–8 mm. The observations were made in wobbler-switching mode with a wobbler throw of 240″. Pointing was checked almost every hour on nearby quasars, planets, or bright HII regions. The data were calibrated with the chopper wheel technique (see Kutner & Ulich 1981), with a calibration uncertainty of about 10% . The spectra were obtained in antenna temperature units, T_A^*, and then converted into main beam brightness temperature, T_{MB}, via the relation $T_A^* = T_{MB}(B_{eff}/F_{eff}) = T_{MB}\eta_{MB}$, where $\eta_{MB} = B_{eff}/F_{eff}$ is the ratio between the main beam efficiency (B_{eff}) of the telescope and the forward efficiency of the telescope (F_{eff}). The spectra were obtained with the fast Fourier transform spectrometers with the finest spectral resolution (FTS50), providing a channel width of 50 kHz. All calibrated spectra were analysed using the GILDAS[1] software developed at the IRAM and the Observatoire de Grenoble. Baselines in the spectra were all fitted by constant functions or polynomials of order 1. The rest frequencies used for the line identification were taken from different laboratory works: HC^{15}N from Cazzoli et al. (2005), H^{13}CN from Cazzoli & Puzzarini (2006), HN^{13}C from van der Tak et al. (2009), H^{15}NC from Pearson et al. (1976), and DNC from Bechtel et al. (2006). The other spectroscopic parameters used to derive the column densities were taken from the Cologne Molecular Database for Spectroscopy[2] (CDMS; Müller et al. 2001, 2005), except for H^{15}NC, for which we have used the Jet Propulsion Laboratory database[3].

3. Results

3.1. H^{15}NC, HN^{13}C, HC^{15}N, and H^{13}CN

The H^{15}NC(1–0) line was detected in 26 cores (96.3%): 11 HMSCs, 8 HMPOs and 7 UC HIIs; the HC^{15}N(1–0) line was detected in 24 cores (88.8%): 8 HMSCs, 9 HMPOs and 7 UC HIIs; the HN^{13}C(1–0) line was detected in all sources (100%), and the H^{13}CN(1–0) line was also clearly detected in all sources (100%).

To evaluate the isotopic ratios, we first of all used the ^{13}C-bearing species of HCN and HNC because the main isotopologues are usually optically thick (e.g. Padovani et al. 2011). Then, we derived the ^{14}N/^{15}N ratio by correcting for the ^{12}C/^{13}C ratio. This latter was derived from the relation between this ratio and the source Galactocentric distance found for CN by Milam et al. (2005). Galactocentric distances were taken from Fontani et al. (2014, 2015a).

Neither H^{15}NC(1–0) nor HC^{15}N(1–0) have hyperfine structure, therefore all the lines were fitted with a single Gaussian. Conversely, HN^{13}C(1–0) and H^{13}CN(1–0) do have hyperfine structure. This cannot be resolved for the HN^{13}C(1–0) because the line widths are always comparable to (or larger than) the separation in velocity of the hyperfine components. Then all the lines were also fitted with single Gaussians, and since the column densities are derived from the total integrated area of the rotational line, this simplified approach does not affect our measurements as long as the lines are optically thin, which is discussed in this section. On the other hand, it can overestimate the intrinsic line width. To estimate by how much, we fitted a line both with the Gaussian and the hyperfine method, and we found that with a single Gaussian, the line width is about 30% larger than is obtained with the hyperfine structure.

Moreover, the fit using the hyperfine method demonstrated that the lines are optically thin. Finally, for H^{13}CN(1–0), for which we were able to resolve the hyperfine structure, we fitted the components simultaneously, assuming that they have the same excitation temperature (T_{ex}) and line width, and that the separation in velocity is fixed to the laboratory value. This fitting procedure gave good results in all spectra. The Gaussian fitting results are listed in Tables A.1 and A.2, and the hyperfine fitting results are listed in Table A.3. In Figs. B.1–B.4 we show the spectra of the H^{15}NC, HC^{15}N, HN^{13}C, and H^{13}CN(1-0) lines for all the 27 sources. The hyperfine components of H^{13}CN(1–0) were always detected. The spectra of AFGL5142-EC may be partially contaminated from the nearby core AFGL5142-mm, but this emission is not expected to be dominant because the angular separation between the two cores is 30″ (Busquet et al. 2011), the same as the beam of the telescope.

The total column densities of the four species averaged within the beam were evaluated from the total line-integrated intensity using Eq. (A4) of Caselli et al. (2002), which assumes that T_{ex} is the same for all transitions within the same molecule, and for optically thin conditions. The assumption of optically thin lines is justified because from all the hyperfine fits of H^{13}CN(1–0) we find $\tau \ll 1$ and well-constrained ($\Delta\tau/\tau \leq 1/3$). We assume that the lines of the other isotopologues are also optically thin. We assume local thermal equilibrium (LTE) conditions, as all the observed sources have average H_2 volume densities of the order of $\sim 10^5$ cm^{-3} (see Fontani et al. 2011, and references therein), that is, comparable to or marginally lower than the critical densities of the observed lines, thus this assumption is also reasonable. Because T_{ex} cannot be deduced from our optically thin spectra (and also because we have only one transition), we adopted as T_{ex} the kinetic temperatures given by Fontani et al. (2011), who derived them following the method described in Tafalla et al. (2004) based on Monte Carlo models, from which they obtained a relation among the kinetic temperature, T_k, and the NH_3 rotation temperature between metastable levels. The T_k values are given in the last column of Tables 3 and 4. This last assumption is critical for the single column densities, but the HN^{13}C/H^{15}NC and H^{13}CN/HC^{15}N column density ratios do not change significantly by varying T_k between 20 and 100 K: changes are of one per cent or of ten percent, depending

[1] The GILDAS software is available at http://www.iram.fr/IRAMFR/GILDAS
[2] http://www.astro.uni-koeln.de/cdms
[3] https://spec.jpl.nasa.gov/

Table 3. Total column densities (beam averaged), computed as explained in Sect. 3, of $H^{15}NC$, $HN^{13}C$, and DNC.

Source	N($H^{15}NC$) ($\times10^{10}$ cm^{-2})	ΔN	N($HN^{13}C$) ($\times10^{11}$ cm^{-2})	ΔN	N(DNC) (10^{11} cm^{-2})	$\frac{HNC}{H^{15}NC}$ *	$\frac{HNC}{DNC}$ **	$\frac{DNC}{HNC}$	T_k (K)
				HMSC					
I00117-MM2	12 ± 4	2	8 ± 1	0.4	4.2 ± 0.6	460 ± 80	406 ± 77	(2.5 ± 0.5) × 10^{-3}	14
AFGL5142-EC^{w}	104 ± 20	10	56 ± 7	1	19 ± 3	398 ± 39	674 ± 136	(1.5 ± 0.3) × 10^{-3}	25
05358-mm3^{w}	141 ± 24	10	74 ± 9	1	27 ± 3	388 ± 28	627 ± 103	(1.6 ± 0.3) × 10^{-3}	30
G034-G2(MM2)	26 ± 8	5	19 ± 3	0.6	4.8 ± 0.7	365 ± 71	612 ± 131	(1.6 ± 0.3) × 10^{-3}	16*
G034-F1(MM8)	19 ± 4	2	20 ± 4	2	2.9 ± 0.4	495 ± 72	1002 ± 243	(1.0 ± 0.2) × 10^{-3}	16*
G034-F2(MM7)	6 ± 3	2	10 ± 1	0.4	1.6 ± 0.3	783 ± 263	908 ± 193	(1.1 ± 0.2) × 10^{-3}	16*
G028-C1(MM9)	43 ± 8	4	28 ± 6	2	3.2 ± 0.8	260 ± 30	1081 ± 356	(0.9 ± 0.3) × 10^{-3}	17
G028-C3(MM11)	13 ± 4	2	11 ± 1	0.4	1.0 ± 0.3	338 ± 53	1360 ± 426	(0.7 ± 0.2) × 10^{-3}	17
I20293-WC	24 ± 7	4	17 ± 4	2	10 ± 1	439 ± 90	326 ± 83	(3.1 ± 0.8) × 10^{-3}	17
I22134-G^{w}	43 ± 8	4	23 ± 3	0.5	4.4 ± 0.6	369 ± 35	1114 ± 210	(0.9 ± 0.2) × 10^{-3}	25
I22134-B	10 ± 3	2	6.0 ± 0.9	0.3	1.3 ± 0.2	414 ± 85	984 ± 211	(1.0 ± 0.2) × 10^{-3}	17
				HMPO					
I00117-MM1	16 ± 4	3	9 ± 1	0.4	3.0 ± 0.5	388 ± 75	640 ± 128	(1.6 ± 0.3) × 10^{-3}	20
AFGL5142-MM	147 ± 24	9	86 ± 10	1	39 ± 5	433 ± 27	504 ± 87	(2.0 ± 0.3) × 10^{-3}	34
05358-mm1	154 ± 25	9	97 ± 11	2	25 ± 3	466 ± 29	887 ± 146	(1.1 ± 0.2) × 10^{-3}	39
18089–1732	58 ± 34	29	52 ± 14	9	12 ± 2	385 ± 204	576 ± 182	(1.7 ± 0.5) × 10^{-3}	38
18517+0437	130 ± 21	8	89 ± 10	1	25 ± 3	349 ± 21	561 ± 92	(1.8 ± 0.3) × 10^{-3}	40*
G75-core	124 ± 31	18	109 ± 16	5	10 ± 1	554 ± 84	2122 ± 377	(5.0 ± 0.9) × 10^{-4}	96
I20293-MM1	103 ± 17	7	80 ± 9	1	12 ± 2	481 ± 33	1277 ± 257	(0.8 ± 0.1) × 10^{-3}	36
I21307	≤15^{u}	–	7 ± 1	0.6	2.1 ± 0.4	≥317	700 ± 167	(1.4 ± 0.4) × 10^{-3}	21
I23385	19 ± 7	5	15 ± 3	2	2.4 ± 0.6	639 ± 189	1564 ± 501	(0.6 ± 0.2) × 10^{-3}	37
				UC HII					
G5.89-0.39	576 ± 70	13	453 ± 49	3	33 ± 4	432 ± 10	2333 ± 379	(4.3 ± 0.7) × 10^{-4}	32*
I19035-VLA1	54 ± 16	10	57 ± 7	2	6 ± 1	570 ± 107	1585 ± 328	(0.6 ± 0.1) × 10^{-3}	39
19410+2336	74 ± 11	4	55 ± 6	0.6	15 ± 2	431 ± 24	657 ± 113	(1.5 ± 0.3) × 10^{-3}	21
ON1	149 ± 21	6	116 ± 12	0.9	22 ± 2	467 ± 19	978 ± 135	(1.0 ± 0.1) × 10^{-3}	26
I22134-VLA1	53 ± 11	6	28 ± 4	0.9	6.3 ± 0.9	364 ± 43	948 ± 191	(1.1 ± 0.2) × 10^{-3}	47
23033+5951	82 ± 15	7	44 ± 5	0.9	8.1 ± 0.9	397 ± 35	1242 ± 197	(0.8 ± 0.1) × 10^{-3}	25
NGC 7538-IRS9	100 ± 21	11	46 ± 6	1	9 ± 1	331 ± 37	1137 ± 195	(0.9 ± 0.1) × 10^{-3}	32*

Notes. In the third and fifth columns we list the error on column densities without considering the calibration error (ΔN). In the seventh, eighth, and ninth columns we list the corresponding $^{14}N/^{15}N$ and D/H isotopic ratios. Uncertainties in the column densities and in the isotope ratios have been computed as explained in Sects. 3.1 and 3.2. In the last column we list the kinetic temperatures of the clumps derived from Fontani et al. (2015a): for the sources without a derivation of T_k, the mean value for that evolutionary stage was taken (for the HMSCs the average was computed without the "warm" ones, i.e. those with T_k < 20 K). (*) Multiplied by $\frac{^{12}C}{^{13}C}$ as described in Sect. 3.1 and given in Table C.1; (**) multiplied by $\frac{^{12}C}{^{13}C}$ and by the correction for the different beams 3.09; (t) tentative detection; (u) upper limits; (w) "warm" HMSC; * average value for the specific evolutionary stage.

on the source. All the column densities and the parameters used to derive them (line integrated intensities) are given in Tables 3 and 4. We consider lines with $T_{MB}^{peak} \geq 3\sigma$ as detections. For the lines that are not clearly detected, we distinguished between those with $2.5\sigma \leq T_{MB}^{peak} < 3\sigma$, and those with $T_{MB}^{peak} < 2.5\sigma$. For the first lines, considered as tentative detections, we computed the total column densities as explained above, and for the latter lines we give an upper limit to the integrated areas and hence to the total column densities using

$$\int T_{MB}\, dv = \frac{\Delta v_{1/2} T_{MB}^{peak}}{2\sqrt{\frac{\ln 2}{\pi}}},$$

where σ is the rms of the spectra, T_{MB}^{peak} is taken equal to 3σ, and $\Delta v_{1/2}$ is the average value of the FWHM of the lines that are clearly detected for the corresponding transition and evolutionary stage of the source. The average value $\Delta v_{1/2}$ for the high-mass starless cores in our data is $\Delta v_{HMSC} = 2.2 \pm 0.3$ km s^{-1}, while for the high-mass protostellar objects, it is $\Delta v_{HMPO} = 1.8 \pm 0.2$ km s^{-1}. Finally, we have derived the column density uncertainties from the errors on the line areas for optically thin lines, given by $\sigma \times \Delta v \times \sqrt{N}$ (σ = rms noise in the spectrum, Δv = spectral velocity resolution, and N = number of channels with signal) and taking into account the calibration error (10%) for the T_{MB}. Conversely, uncertainties in the $^{14}N/^{15}N$ ratios were computed from the propagation of errors on the column densities, as explained above, without taking the calibration uncertainties into account because the lines were observed in the same spectrum (see Sect. 2), so that the calibration error cancels out in their ratio.

3.2. DNC

We also detected the rotational transition DNC(2–1) for all the 27 sources. These lines are used to measure the D/H ratio, which

Table 4. Total column densities (beam averaged), computed as explained in Sect. 3, of $HC^{15}N$ and $H^{13}CN$(1–0) transitions.

Source	N($HC^{15}N$) ($\times10^{10}$ cm^{-2})	ΔN	N($H^{13}CN$) ($\times10^{11}$ cm^{-2})	ΔN	$\frac{HCN}{HC^{15}N}$ *	T_k (K)
HMSC						
I00117-MM2	22 ± 6	4	9 ± 1	0.5	282 ± 54	14
AFGL5142-EC^{w}	327 ± 47	14	176 ± 20	2	398 ± 18	25
05358-mm3^{w}	270 ± 39	12	158 ± 18	2	433 ± 20	30
G034-G2(MM2)	≤17^{u}	–	5 ± 1	0.3	≥ 147	16*
G034-F1(MM8)	14 ± 4	3	11 ± 2	0.4	369 ± 80	16*
G034-F2(MM7)	≤14^{u}	–	5 ± 1	0.3	≥ 168	16*
G028-C1(MM9)	32 ± 9^{t}	6	23 ± 3	0.7	287 ± 55	17
G028-C3(MM11)	≤16^{u}	–	10 ± 2	0.8	≥250	17
I20293-WC	31 ± 12	9	31 ± 4	0.6	620 ± 180	17
I22134-G^{w}	120 ± 17	5	56 ± 6	0.8	322 ± 14	25
I22134-B	17 ± 4	2	10 ± 1	0.4	406 ± 50	17
HMPO						
I00117-MM1	38 ± 8	4	19 ± 2	0.6	345 ± 38	20
AFGL5142-MM	558 ± 70	14	292 ± 31	2	387 ± 10	34
05358-mm1	351 ± 50	14	205 ± 23	2	432 ± 18	39
18089–1732	354 ± 36	9	278 ± 30	2	338 ± 9	38
18517+0437	405 ± 52	11	259 ± 28	2	326 ± 9	40*
G75-core	790 ± 88	9	324 ± 35	2	258 ± 3	96
I20293-MM1	187 ± 28	9	152 ± 17	2	504 ± 25	36
I21307	35 ± 7	4	20 ± 3	0.7	389 ± 46	21
I23385	134 ± 26	12	48 ± 6	0.9	290 ± 26	37
UC HII						
G5.89-0.39	1674 ± 246	81	775 ± 79	2	255 ± 12	32*
I19035-VLA1	157 ± 28	12	99 ± 11	2	340 ± 27	39
19410+2336	176 ± 23	5	123 ± 13	1	405 ± 12	21
ON1	319 ± 40	8	174 ± 18	1	327 ± 8	26
I22134-VLA1	152 ± 22	7	86 ± 10	1	390 ± 18	47
23033+5951	155 ± 23	7	96 ± 11	1	458 ± 21	25
NGC 7538-IRS9	288 ± 43	14	164 ± 18	1	410 ± 20	32*

Notes. In the third and fifth columns we list the error on column densities without considering the calibration error (ΔN). In the sixth column we list the corresponding $^{14}N/^{15}N$ isotopic ratios. Uncertainties have been derived as explained in the caption of Table 3. In the last column we list the kinetic temperatures of the clumps derived from Fontani et al. (2015a). $^{(*)}$ Multiplied by $\frac{^{12}C}{^{13}C}$ as described in Sect. 3.1 and given in Table C.1; $^{(t)}$ tentative detection; $^{(u)}$ upper limits; $^{(w)}$ "warm" HMSC; * average value for the specific evolutionary stage.

is compared with the $^{14}N/^{15}N$ ratio. Such a high detection rate indicates that deuterated gas is present at every stage of the massive star and star cluster formation process, as has been noted by Fontani et al. (2011). The transition possesses a hyperfine structure that is not resolved because of the broad line widths (see Table A.2). Therefore the lines where fitted with a single Gaussian. To estimates how much the line widths are overestimated using Gaussian fits, we fitted a line both with the Gaussian and the hyperfine method, and we found that with a single Gaussian, the line width is about 10% larger than that obtained with the hyperfine structure. We point out that for evolved sources (HMPOs and UC HIIs) another line in the spectra partly overlaps DNC(2-1). This is identified as acetaldehyde at 152.608 GHz (the $J_{Ka,Kc} = 8_{0,8}-7_{0,7}$ transition). The fact that the line is only detected in the evolved objects is consistent with the idea that acetaldehyde is probably released from grain mantles because it is detected only in warmer and more turbulent objects (see e.g. Codella et al. 2015). When we fitted the DNC lines with Gaussians, we excluded the contribution of this line by fitting the two lines simultaneously, and when possible, we excluded this line from the fit. The fitting results are listed in Table A.2.

We determined the column densities under the assumption of optically thin conditions and the same T_{ex} for all transitions using Eq. (A4) of Caselli et al. (2002) in this case as well,

$$N_{TOT} = \frac{8\pi\nu_{ij}^3}{c^3 A_{ij}} \frac{1}{g_i} \frac{W}{(J_{\nu_{ij}}(T_{ex}) - J_{\nu_{ij}}(T_{BG}))} \frac{1}{\left(1-\exp\left(-\frac{h\nu_{ij}}{kT_{ex}}\right)\right)} \frac{Q(T_{ex})}{\exp\left(-\frac{E_j}{kT_{ex}}\right)}, \quad (1)$$

where ν_{ij} is the transition frequency, A_{ij} is the Einstein coefficient of spontaneous emission, g_i is the statistical weight of the upper level, E_j is the energy of the lower level, c is the speed of light, k is the Boltzmann constant, T_{ex} is the excitation temperature of the transition, $Q(T_{ex})$ is the partition function at temperature T_{ex}, and T_{BG} is the background temperature (2.7 K), $J_{\nu_{ij}}(T)$ is

$$J_{\nu_{ij}}(T) = \frac{h\nu_{ij}}{k} \frac{1}{\exp\left(\frac{h\nu_{ij}}{kT}\right) - 1},$$

W is the integrated intensity of the line ($\int T_B \, dv = (\int T_{MB} \, dv) \frac{\Omega_{MB}}{\Omega_s}$, where T_B is the brightness temperature, Ω_{MB} is

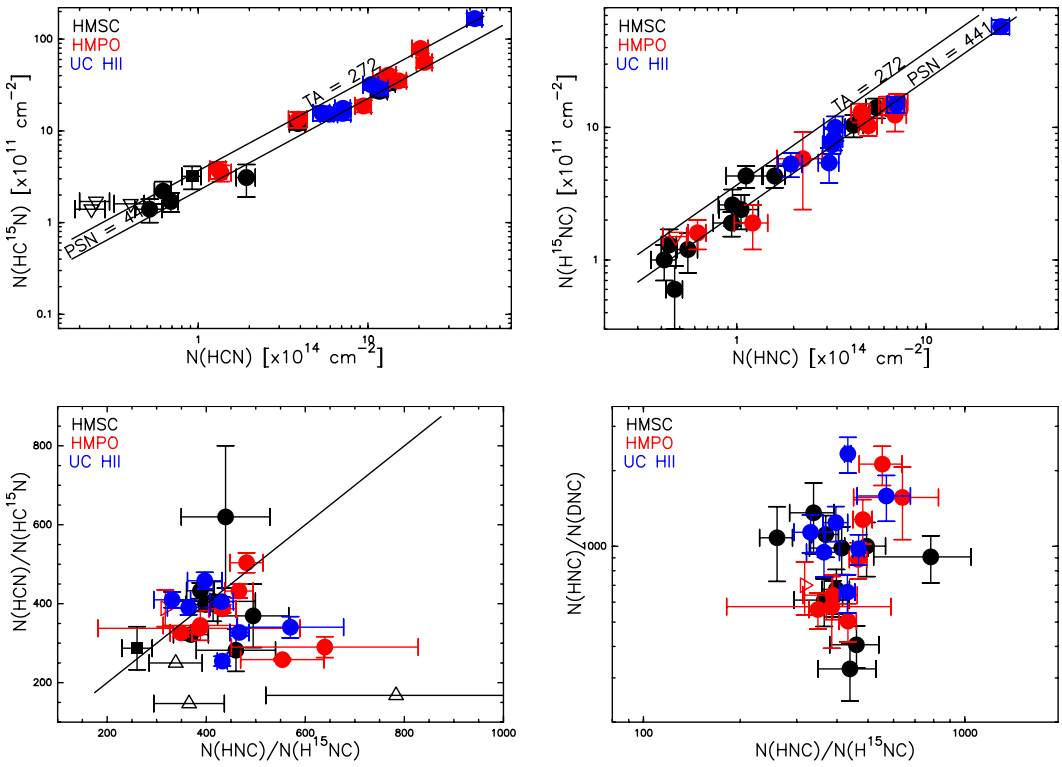

Fig. 1. *Top panels*: column density of HCN compared with that of $HC^{15}N$ (*left*) and of HNC compared with that of $H^{15}NC$ (*right*). *Bottom panels*: comparison between the $^{14}N/^{15}N$ isotopic ratios derived from the column density ratios N(HCN)/N($HC^{15}N$) and N(HNC)/N($H^{15}NC$) (*left*) and comparison between the H/D and $^{14}N/^{15}N$ isotopic ratios in HNC (*right*). In all panels, the filled circles represent the detected sources (black = HMSCs; red = HMPOs; blue = UC HIIs). The open triangles in the top panels are the upper limits on N($H^{15}NC$) (*right*) and N($HC^{15}N$) (*left*), while in the *bottom panels* the open triangles indicate lower limits on either N(HCN)/N($HC^{15}N$) or N(HNC)/N($H^{15}NC$). The filled squares represent tentative detections. The solid lines in the top panels indicate the mean atomic composition as measured in the terrestrial atmosphere (TA) and in the protosolar nebula (PSN), while in the *bottom left panel*, the solid line indicates the locus of points where N(HCN)/N($HC^{15}N$) is equal to N(HNC)/N($H^{15}NC$).

the solid angle of the main beam, and Ω_s is the solid angle of the source). However, in this case, the HNC/DNC ratio depends on the temperature because of the different excitation conditions of the two transitions observed ((2–1) for DNC and (1–0) for $HN^{13}C$), so that the ratio depends on the temperature by the factor $\exp(E_j/kT)$. We also corrected the HNC/DNC ratios for the different beams of the antenna at the frequencies of the two lines, and we assumed that the emissions of DNC(2–1) and HNC(1–0) are less extended than the beam size of DNC(2–1). This last correction results in a factor 3.09 that is to be multiplied with the HNC/DNC ratio:

$$\left(\frac{1.22\frac{\lambda_1}{D}}{1.22\frac{\lambda_2}{D}}\right)^2 = \left(\frac{\lambda_1}{\lambda_2}\right)^2 = \left(\frac{\nu_2}{\nu_1}\right)^2 = 3.09,$$

where λ_1 and λ_2 are the wavelengths of the HNC(1–0) and DNC(2–1) transitions, respectively (and ν_1 and ν_2 are the corresponding frequencies). In Fig. B.5 we show the spectra of DNC(2–1) for all the 27 sources. The total column densities are listed in Table 3. Finally, we derived the errors as explained in Sect. 3.1, but here for the D/H ratios we also considered the calibration uncertainties because the two lines were observed in separate setups.

4. Discussion

4.1. ^{15}N-fractionation

The comparison between the column densities of the ^{15}N-containing species and those of their main isotopologues, derived as explained in Sect. 3, is shown in Fig. 1. The corresponding $^{14}N/^{15}N$ ratios are given in Tables 3 and 4.

We first discuss the ^{15}N-fractionation found for HCN. The top left panel in Fig. 1 shows no large spread of measured values, which are very similar to the value found for the PSN. The mean values for the three evolutionary stages are 346 ± 37 for HMSCs, 363 ± 25 for HMPOs, and 369 ± 25 for UC HIIs. Although the HMSCs have the highest ^{15}N-enrichment, the mean values for the three evolutionary categories are however consistent within the errors, which indicates that time does not seem to play a role in the fractionation of nitrogen (at least until the formation of a HII region). In the top panels of Fig. 2 we show the $^{14}N/^{15}N$ ratios calculated for HCN in the 27 sources as a function of the Galactocentric distance, of the line width, and of the kinetic temperature, respectively: again, there is no evidence of a trend of these ratios with any of the adopted parameters. In particular, the lack of correlation with either temperature or line width, which are both thought to increase with the evolution of the source, confirms the independence of the $^{14}N/^{15}N$ ratio from the core age. The lack of correlation with evolutionary parameters was also found by Fontani et al. (2015a) in N_2H^+, but the dispersion of the ratios is clearly much smaller in our study (from 180 up to 1300 in Fontani et al. 2015a, and from 250 up to 650 in this work). The reason may also be that they have larger uncertainties on average.

We now examine the ^{15}N- fractionation found for HNC: we do not find a large spread of values here either compared with the results reported in Fontani et al. (2015a). The $^{14}N/^{15}N$ ratios are distributed within ~250 and 630 (top right panel in Fig. 1).

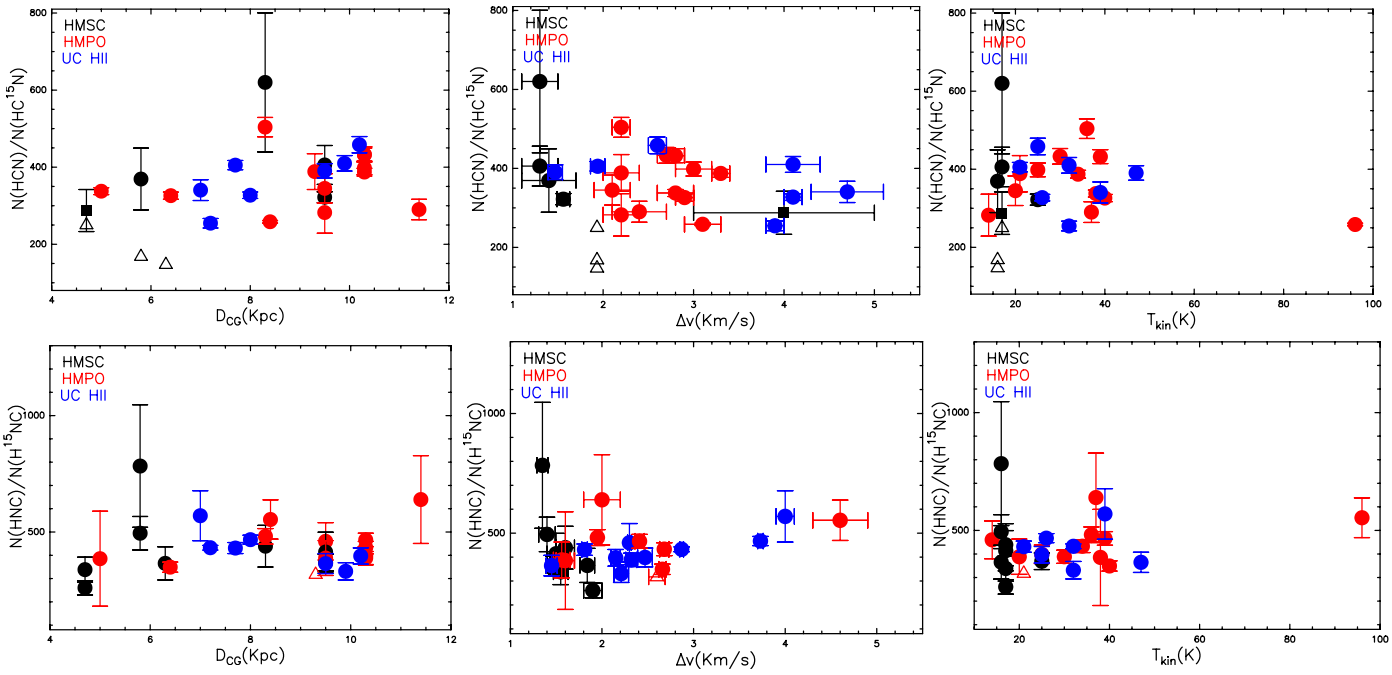

Fig. 2. *Top panels*: N(HCN)/N(HC^{15}N) as a function of Galactocentric distances, line widths, and kinetic temperatures. *Bottom panels*: N(HNC)/N(H^{15}NC) as a function of Galactocentric distances, line widths, and kinetic temperatures. The symbols are the same as in the bottom panels of Fig. 1.

The mean values for the three evolutionary stages are 428 ± 40 for HMSCs, 462 ± 31 for HMPOs, and 428 ± 29 for UC HIIs, which is consistent within the errors with the ^{14}N/^{15}N ratio measured for the PSN of about 441 (from the solar wind). For this molecule, no trend between the isotopic ratio and either the line width or the kinetic temperature was found either (bottom panels of Fig. 2). In conclusion, time does not seem to play a role for either ratio.

The lack of correlation between the ^{14}N/^{15}N isotopic ratios and evolutionary parameters or physical parameters (FWHM, T_k) are somewhat consistent with the chemical model of Roueff et al. (2015), who predicted no fractionation of HCN and HNC in cold and dense conditions. However, their models are more appropriate for low-mass dense cores, with a T_k of 10 K, than for the warmer high-mass pre-stellar objects of the type studied in this work. This may explain the lack of carbon fractionation in our work, which is in contrast to their predictions. We stress that ^{13}C may in theory have reduced abundances because nitriles and isonitriles are predicted to be significantly depleted in ^{13}C (Roueff et al. 2015). However, this depletion is at most of a factor 2 (see Fig. 4 in Roueff et al. 2015) and is derived from a chemical model with a fixed kinetic temperature of 10 K, which is not the average kinetic temperature of our sources (not even of the starless cores, see Table 3). The predictions of this model may therefore not be appropriate for our objects. Furthermore, the ^{13}C-fractionation is dependent on the time and temperature evolution (Szűcs et al. 2014; Röllig & Ossenkopf 2013), and observational tests to verify whether this theoretical effect is real have yet to be performed.

Intriguingly, when we performed a Kolmogorov-Smirnov test, which is a non-parametric statistical test, to determine whether the two data sets (the first set is the HC^{14}N/HC^{15}N ratios and the second is the H^{14}NC/H^{15}NC ratios) belong to the same distributions, we found a P-value = 0.078. The test indicates independence only if $P \leq 0.05$, and this could mean that we cannot conclude anything about the dependence or the independence of the two samples with our results. It is known from the literature that H^{15}NC and HC^{15}N can form through the same reactions (see Terzieva & Herbst 2000; Wirström et al. 2012). We also checked the H^{15}NC/HC^{15}N column density ratio, and we found that it is roughly more than 1 for HMSCs (with an average value of $\sim 1 \pm 0.5$) and roughly less than 1 for HMPOs and UC HIIs (with an average value of $\sim 0.3 \pm 0.1$). Loison et al. (2014) showed that in cold regions, where C and CO are depleted, the dissociative recombination of HCNH$^+$ acts to isomerize HCN into HNC, producing HCN/HNC ratios close to or slightly above one. In hot gas, the CN + H_2 reaction with its high activation energy (2370 K; Jacobs et al. 1989) and the isomeration process C + HNC → C + HCN (Loison et al. 2014) may be responsible for the high HCN/HNC measured in hot cores (Schilke et al. 1992) and in young stellar objects (Schöier et al. 2002). That our HC^{15}N/H^{15}NC ratios are always close to one appears to imply that both species are probing similar low-temperature gas.

Interestingly, the ^{14}N/^{15}N ratio measured towards the source HMSC-G034F2 is an outlier (too high) in the distribution of the ratios in both HCN and HNC (but with larger errors than in other objects): a similarly high value was found by Bizzocchi et al. (2013) in L1544, which is a typical low-mass pre-stellar core. In particular, Bizzocchi et al. found a value of ^{14}N/^{15}N $\simeq 1000 \pm 200$ from the N_2H^+. This result, and the results measured in HMSC-G034F2, are not consistent with the predictions of current models on nitrogen chemistry for N_2H^+, HCN, and HNC (Roueff et al. 2015; Hily-Blant et al. 2013a). The ^{14}N/^{15}N ratios in HCN and HNC for cores G028-C1, G034-C3, G028-F2, G034-F1, and G034-G2 have also been studied independently by Zeng et al. (2017), and both works obtain consistent results (within a factor of two). Taking into account HC^{15}N in G028-C1 and comparing our spectrum with that of Zeng et al. (2017) at the same velocity resolution of 0.68 km s^{-1}, we obtained an rms of 0.01 K, while they obtained an rms of 0.02 K. Our T_{MB}^{peak} is 0.03 K, that is, more than 2.5σ, so we can refer to this line as

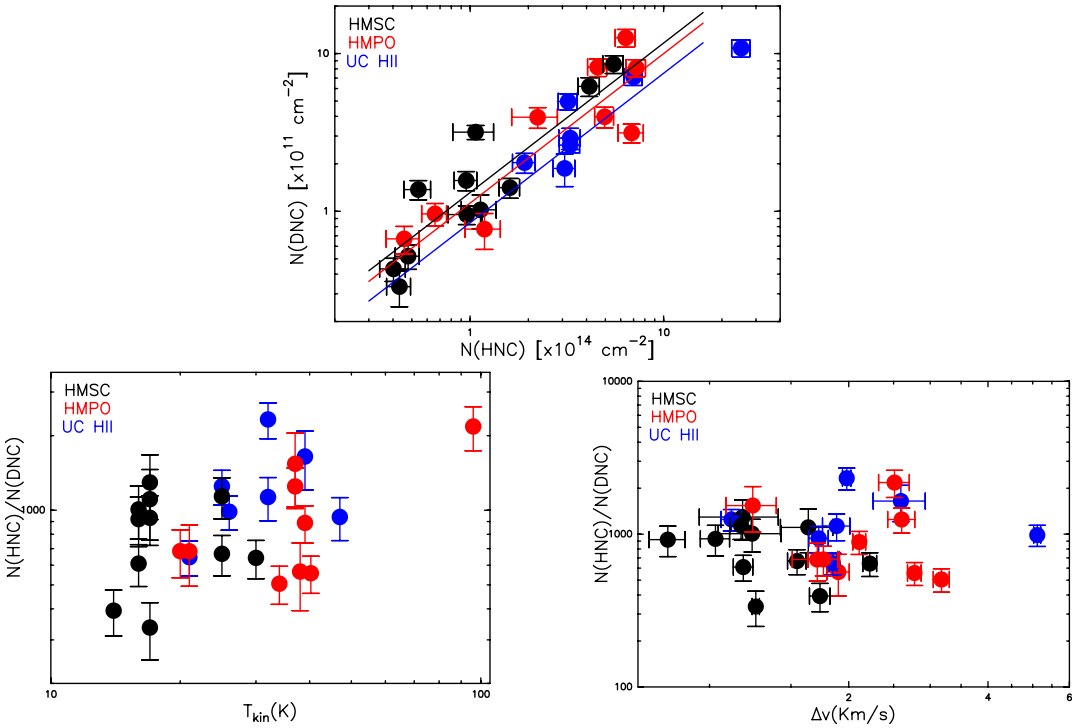

Fig. 3. *Top panel*: column density of HNC compared with that of DNC. The three lines represent the mean values of D/H (see text) for different evolutionary stages: black for HMSCs, red for HMPOs and blue for UC HIIs. *Bottom panels*: N(HNC)/N(DNC) as a function of line widths and kinetic temperatures. The filled circles have the same meaning as in Fig. 1.

a tentative detection, while Zeng et al. (2017) reported an rms that is comparable with the peak of our line. They also derived the upper limit of the column density using a $\Delta v_{1/2}$ of the line of 2 km s^{-1}, while with our fit we obtained a $\Delta v_{1/2}$ of 4 km s^{-1}: this is the reason for the factor 2 of difference in the integrated area of this line in the two works. This effect is the same in the other spectra (compare Figs. A1–A3 of their work with our Figs. B1–B4), and the different integrated areas are also due to the different resolution and sensitivity.

4.2. D-fractionation

The top panel of Fig. 3 shows the comparison between the column densities of DNC and HNC, derived as explained in Sect. 3. The N(HNC)/N(DNC) mean values obtained for the three evolutionary stages are 823 ± 94 for HMSCs, 983 ± 189 for HMPOs, and 1275 ± 210 for UC HIIs, indicated by three different lines in Fig. 3. Accordingly, the D/H mean ratios are $(1.4 \pm 0.2) \times 10^{-3}$ for HMSCs, $(1.3 \pm 0.2) \times 10^{-3}$ for HMPOs, and $(0.9 \pm 0.1) \times 10^{-3}$ for UC HIIs. The D/H mean values were obtained from computing the average for all the D/H values (Table 3). We note that the D/H values are slightly higher in the early stages, but because of the large dispersions, the differences between the three evolutionary categories are not statistically significant. This result confirms the marginally decreasing trend found by Fontani et al. (2014), derived from the DNC (1–0) transition in a subsample of the sources observed in this work. Fontani et al. (2014) found an average D/H of 0.012, 0.009, and 0.008 in HMSCs, HMPOs, and UC HIIs, respectively, with no statistically significant differences among the three evolutionary groups.

4.3. Comparison between D/H and $^{14}N/^{15}N$

Considering the D- and N-fractionation for HNC towards the same sources, we can find an indication as to whether the two fractionations are linked. The bottom right panel in Fig. 1 shows HNC/DNC as a function of HNC/H^{15}NC. The data show an independence between the two data sets, and this can be shown by computing the Kendall τ test. This is a non-parametric test used to measure the ordinal association between two data sets; its definition is

$$\tau = \frac{(\#\text{ concordant pairs}) - (\#\text{ discordant pairs})}{\frac{n(n-1)}{2}},$$

with n the number of the total pairs. If $\tau = 1$, there is a full correlation, if $\tau = -1$, there is full anti-correlation, and if $\tau = 0$, the two data sets are independent. We chose this statistical test because compared to other non-parametric tests (i.e. the Spearman ρ correlation coefficient), this test is more robust; moreover, it allows us to compare our analysis with that performed by Fontani et al. (2015a), who used the same test. Following this, we computed τ for the two data sets HNC/DNC and HNC/H^{15}NC, and we found $\tau \sim 0.13$, which means that the D- and ^{15}N- fractionation in these sources for HNC are independent. This result must be compared with that of Fontani et al. (2015a), which suggested a possible anti-correlation between the two isotopic ratios for N_2H^+. This finding arises mostly from the fact that the $^{14}N/^{15}N$ ratio does not vary with the core evolution, while the D-fractionation shows a faint decreasing trend. This result indicates that the parameters that cause D-enrichment in HCN and HNC may not influence the fractionation of nitrogen. The independence we found reflects what has been found in some pristine solar system material, in which the spots of high D-enrichments are not always spatially coincident with those with high ^{15}N enrichment. From the point of view of the models, as discussed in Wirström et al. (2012), the D- and ^{15}N-enrichments do not need to be spatially correlated (although they could be produced by the same mechanism, i.e. exothermic reactions due to the different zero-point energy of the heavier isotope), because relevant

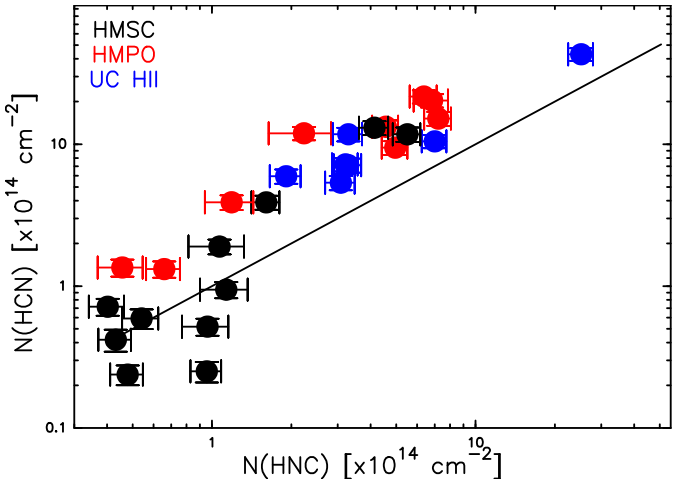

Fig. 4. Column density of HCN compared with that of HNC. The solid line is the locus where N(HCN)/N(HNC) is equal to 1, as statistically expected. The filled circles have the same meaning as in Fig. 1.

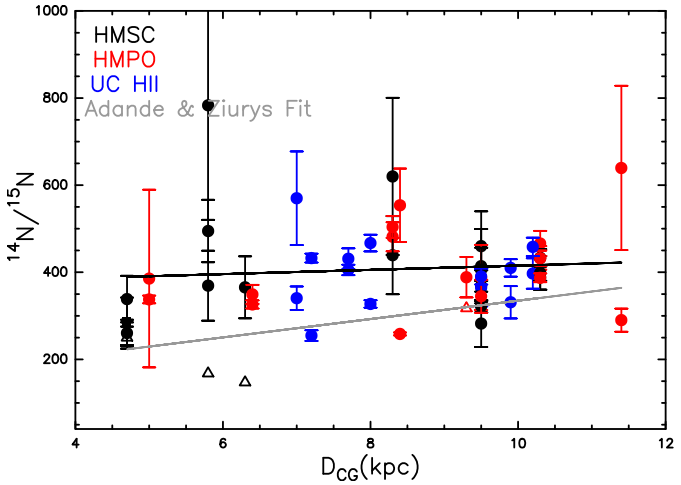

Fig. 5. $^{14}N/^{15}N$ ratios as a function of Galactocentric distances (for HNC and HCN together). The symbols are the same as in the bottom panels of Fig. 1. The black line is the linear fit computed for the plotted data, and the grey line represents the fit of Adande & Ziurys (2012).

reactions for D- and ^{15}N-enrichments have different energy barriers. Roueff et al. (2015) recently reviewed some of the reactions in ^{15}N-fractionation, and based on the model, concluded that other modeling work is necessary to fully understand the relation of the two fractionation processes.

4.4. Comparison between N(HNC) and N(HCN)

For completeness, we also calculated the ratio between N(HNC) and N(HCN). Figure 4 shows the column density of HCN versus HNC, and we immediately note that HMSCs show values of HCN/HNC $\lesssim 1$ unlike HMPOs and UC HIIs, for which the ratio is >1. The mean values are 0.8 $\pm$0.2 for HMSCs, 2.5 $\pm$0.2 for HMPOs, and 2.0 $\pm$ 0.2 for UC HIIs.

We computed the HNC/HCN ratio in the two data sets of HMSCs and HMPOs+UC HIIs. Using the non-parametric statistical Kolmogorov-Smirnov test, we obtain a P-value = 0.025, which indicates that the two distributions are different. Schilke et al. (1992) reported predictions and observations for the Orion hot core OMC-1, which is the prototype of a high-mass hot core. They found that the HCN/HNC abudance ratio is very high (~80) in the vicinity of Orion-KL, but it rapidly declines in positions adjacent to values of ~5. They compared the observations with the predictions of molecular cloud chemistry and found an agreement with steady-state models. More recently, Jin et al. (2015) found that the abundance ratio increases if the sources evolved from IRDCs to UC HIIs, and they suggested that this might occur for neutral-neutral reactions where HNC is selectively consumed for $T \gtrsim 24$ K (Hirota et al. 1998):

$$\mathrm{HNC + H \rightarrow HCN + H;}$$

$$\mathrm{HNC + O \rightarrow NH + CO.}$$

For the first reaction, a 2000 K barrier was found, and the second barrier has not yet been theoretically and experimentally studied, but if it were possible, N(HNC)/N(HCN) would decrease rapidly in warm gas. We therefore emphasize the importance of future laboratory measurements of these later reactions, especially at low temperatures.

4.5. Comparison with the $^{14}N/^{15}N$ Galactocentric gradient

Adande & Ziurys (2012) evaluated the $^{14}N/^{15}N$ ratio across the Galaxy through millimetre observations of CN and HNC in regions of star formation. They also enlarged the sample with the high-mass sources observed by Dahmen et al. (1995) via HCN observations. In order to compare our results with their work, we have plotted our $^{14}N/^{15}N$ ratios (for HCN and HNC together) as a function of the Galactocentric distance of the sources (see Table C.1 and Fig. 5). We computed a linear fit and obtained the relation

$$^{14}\mathrm{N}/^{15}\mathrm{N} = (4.9 \pm 7.6)\ \mathrm{kpc}^{-1} \times D_{\mathrm{GC}} + (366.5 \pm 65.6), \quad (2)$$

which disagrees with the relation obtained by Adande & Ziurys (2012),

$$^{14}\mathrm{N}/^{15}\mathrm{N} = (21.1 \pm 5.2)\ \mathrm{kpc}^{-1} \times D_{\mathrm{GC}} + (123.8 \pm 37.1). \quad (3)$$

This indicates that our data set does not confirm the gradient found by Adande & Ziurys (2012). We speculate that as the beam used by Adande & Ziurys (2012) is larger and hence more influenced by the diffuse surrounding material, the difference in ratios may be due to the material surrounding the target cores, in which this ratio may be lower. We also note that Adande & Ziurys (2012) derived their fit using the source SgrB2(NW), which is located at a Galactocentric radius of 0.1 kpc: for this source, they obtained a $^{14}N/^{15}N$ lower limit of 164. This value strongly influences their fit results and hence could have a strong effect on both the slope and the intercept with the y-axis. Any comparison between the two fit results must therefore be taken with caution.

5. Conclusions

We have observed the $J = 1$–0 rotational transitions of $H^{15}NC$, $HN^{13}C$, $H^{13}CN$, and $HC^{15}N$ together with the $J = 2$–1 transition of DNC towards 27 massive star-forming cores in different evolutionary stages in order to derive the ^{15}N- and D-fractionation, and to compare the ratios with each other. We find $^{14}N/^{15}N$ in HCN between ~200 and ~700, and in HNC between ~260 and ~600, with a small spread around the PSN value of 441. Comparing the $^{14}N/^{15}N$ ratios for different evolutionary stages, we

did not find any trend, indicating that time does not seem to play a role in the N-fractionation; furthermore, we cannot conclude about the correlation between the ^{15}N-fractionation for the two molecules HNC and HCN. Considering both D- and ^{15}N-fractionation for HNC towards the same sources, we found no correlation. This is consistent with the lack of correlation found by Fontani et al. (2015a) in N_2H^+: the causes of D-enrichment in HCN and HNC do not affect the ^{15}N-fractionation. Our findings are in agreement with the recent chemical models of Roueff et al. (2015). The independence between D/H and ^{14}N/^{15}N ratios confirms the recent findings of Guzmán et al. (2017) in protoplanetary discs. Conversely, the low values of ^{14}N/^{15}N found by them (and the tentative decrease with decreasing distance to the star) does not contradict our findings because our results are obtained on angular scales much larger than that of a protoplanetary disc. All this indicates that the ^{15}N enrichment is a local effect that does not involve the larger-scale envelope.

Acknowledgements. We are grateful to the IRAM-30 m telescope staff for their help during the observations. Many thanks to the anonymous referee for the careful reading of the paper and the comments that improved the work. Paola Caselli acknowledges support from the European Research Council (project PALs 320620).

References

Adams, F. C. 2010, ARA&A, 48, 74
Adande, G. R., & Ziurys, L. M. 2012, ApJ, 744, 194
Aléon, J., Engrand, C., Leshin, L. A., & McKeegan, K. D. 2009, Geochim. Cosmochim. acta., 73, 4558
Altwegg, K., Balsiger, H., Bar-Nun, A., et al. 2015, Science, 347, 387
Banerjee, P., Qian, Y.-Z., Heger, A., & Haxton, W. C., et al. 2016, Nat. Commun., 7, 13639
Bechtel, H., Steeves, A., & Field, R. 2006, ApJ, 649, L53
Bizzocchi, L., Caselli, P., Leonardo, E., & Dore, L. 2013, A&A, 555, A109
Bonal, L., Huss, G. R., Nagashima, K., & Krot, A. N. 2009, Meteorit. Planet. Sci. Suppl., 72, 5178
Busemann, H., Young, A. F., & Alexander, C. M. O. D. 2006, Science, 312, 727
Busquet, G., Estalella, R., Zhang, Q., et al. 2011, A&A, 525, A141
Caselli, P., & Ceccarelli, C. 2012, A&ARv, 20, 56
Caselli, P., Walmsley, C. M., Tafalla, M., Dore, L., & Myers, P. C. 1999, ApJ, 523, L165
Caselli, P., Walmsley, C. M., Zucconi, A., et al. 2002, ApJ, 565, 344
Caselli, P., Vastel, C., Ceccarelli, C., et al. 2008, A&A, 492, 703
Cazaux, S., Caselli, P., & Spaans, M. 2011, ApJ, 741, 34
Cazzoli, G., Puzzarini, C., & Gauss, J. 2005, ApJS, 159, 181
Cazzoli, G., Cludi, L., & Puzzarini, C. 2006, J. Mol. Struct., 780, 260
Ceccarelli, C., Caselli, P., Bockelee-Morvan, D., et al. 2014, in Protostars and Planets VI., eds. H. Beuther, R. S. Klessen, C. P. Dullemond, & T. Henning (Tucson: University of Arizona Press), 859
Codella, C., Fontani, F., Ceccarelli, C., et al. 2015, MNRAS, 449, L11
Crapsi, A., Caselli, P., Walmsley, C. M., et al. 2005, ApJ, 619, 379
Dahmen, G., Wilson, T. L., & Matteucci, F. 1995, A&A, 295, 194
Daniel, F., Faure, A., Pagani, L., et al. 2016, A&A, 592, A45
Emprechtinger, M., Caselli, P., Volgenau, N. H., Stutzki, J., & Wiedner, M. C. 2009, A&A, 493, 89
Fontani, F., Palau, A., Caselli, P., et al. 2011, A&A, 529, L7
Fontani, F., Giannetti, A., Beltrán, M. T., et al. 2012, MNRAS, 423, 2342
Fontani, F., Sakai, Furuya, K. T., Sakai, N., Aikawa, Y., & Yamamoto, S. 2014, MNRAS, 440, 448
Fontani, F., Caselli, P., Palau, A., Bizzocchi, L., & Ceccarelli, C. 2015a, ApJ, 808, L46
Fontani, F., Busquet, G., Palau, A., et al. 2015b, A&A, 575, A87
Füri, E., & Marty, B. 2015, Nat. Geosci., 8, 515
Geiss, J., & Gloeckler, G. 1998, Space Sci. Rev., 84, 239
Gerin, M., Marcelino, N., Biver, N., et al. 2009, A&A, 498, L9
Gerlich, D., Herbst, E., & Roueff, E. 2002, Planet. Space Sci., 50, 1275
Guzmán, V. V., Öberg, K. I., Huang, J., Loomis, R., & Qi, C. 2017, ApJ, 836, 15
Hartogh, P., Lis, D. C., Bockelée-Morvan, D., et al. 2011, Nature, 478, 218
Heays, A. N., Visser, R., Gredel, R., et al. 2014, A&A, 562, A61
Hily-Blant, P., Pineau des Forets, G., Faure, A., Le Gal, R., & Padovani, M. 2013a, A&A, 557, A65
Hily-Blant, P., Bonal, L., Faure, A., & Quirico, E. 2013b, Icarus, 223, 582
Hily-Blant, P., Magalhaes, V., Kastner, J., et al. 2017, A&A, 603, L6
Hirota, T., Yamamoto, S., Mikami, H., & Ohishi, M. 1998, ApJ, 503, 717
Hunter, D. A. 2001, ApJ, 559, 225
Hoare, M. G., Kurtz, S. E., Lizano, S., Keto, E., & Hofner, P. 2007, Protostars and Planets IV, 951
Jacobs, A., Wahl, M., Weller, R., et al. 1989, Symp. Int. Combust. Proc., 22, 1093
Jin, M., Lee, J.-E., & Kim, K.-T. 2015, ApJS, 219, 2
Kong, S., Caselli, P., Tan, J. C., Wakelam, V., & Sipilä, O. 2015, ApJ, 804, 98
Kurtz, S., Cesaroni, R., Churchwell, E., Hofner, P., & Walmsley, C. M. 2000, Protostars and Planets IV, 299
Kutner, M. L., & Ulich, B. L. 1981, ApJ, 250, 341
Linsky, J. L., Draine, B. T., Moos, H. W., et al. 2006, ApJ, 647, 1106
Lis, D. C., Phillips, T. G., Goldsmith, P. F., et al. 2010, A&A, 521, L26
Loison, J.-C., Wakelam, V., & Hickson, K. M. 2014, MNRAS, 443, 398
Manfroid, J., Jehin, E., Hutsemékers, D., et al. 2009, A&A, 503, 613
Marty, B., Zimmermann, L., & Burnard, P. G. 2009, Geochim. Cosmochim. Acta, 73, 842
Marty, B., Zimmermann, L., Burnard, P. G., et al. 2010, Geochim. Cosmochim. Acta, 74, 340
Milam, S. N., & Charnley, S. B. 2012, Technical Rep. Lunar and Planetary Institute Science Conference Abstracts, 43, 2618
Milam, S. N., Savage, C., Brewster, M. A., Ziurys, L. M., & Wyckoff, S. 2005, ApJ, 634, 1126
Müller, H. S. P., Thorwirth, S., Roth, D. A., & Winnewisser, G. 2001, A&A, 370, L49
Müller, H. S. P., Schlüder, F., Stutzki, J., & Winnewisser, G. 2005, J. Mol. Struct., 42, 215
Owen, T., Mahaffy, P. R., Niemann, H. B., Atreya, S., & Wong, M. 2001, ApJ, 553, L77
Pagani, L., Salez, M., & Wannier, P. G. 1992, A&A, 258, 479
Padovani, M., Walmsley, C. M., Tafalla, M., Hily-Blant, P., & Pineau Des Forêts, G. 2011, A&A, 534, A77
Pearson, E. F., Creswell, R. A., Winnewisser, M., & Winnewisser, G. 1976, ZNatA, 31a, 1394
Remusat, L., Robert, F., Meibom, A., et al. 2009, ApJ, 698, 2087
Robert, F. 2003, Space Sci. Rev., 106, 87
Robert, F., & Derenne, S. 2006, Meteor. Planet. Sci. Suppl., 41, 5259
Röllig, M., & Ossenkopf, V. 2013, A&A, 550, A56
Roueff, E., Loison, J. C., & Hickson, K. M. 2015, A&A, 576, A99
Schilke, P., Walmsley, C. M., Pineau Des Forets, G., et al. 1992, A&A, 256, 595
Schoier, F. L., Jørgensen, J. K., van Dishoeck, E. F., & Blake, G. A. 2002, A&A, 390, 1001
Shinnaka, Y., Kawakita, H., Jehin, E., et al. 2016, MNRAS, 462, S195
Szűcs, L., Glover, S. C. O., & Klessen, R. S. 2014, MNRAS, 445, 4055
Tafalla, M., Myers, P. C., Caselli, P., & Walmsley, C. M. 2004, A&A, 416, 191
Taquet, V., Ceccarelli, C., & Kahane, C. 2012, A&A, 538, A42
Taquet, V., Peters, P. S., Kahane, C., et al. 2013, A&A, 550, A127
Taquet, V., Furuya, K., Walsh, C., & van Dishoeck, E. F. 2016, MNRAS, 462, 99
Terzieva, R., & Herbst, E. 2000, MNRAS, 317, 563
van der Tak, F. F. S., Müller, H. S. P., Harding, M. E., & Gauss, J. 2009, A&A, 507, 347
Walmsley, C. M., Flower, D. R., & Pineau des Forêts, G. 2004, A&A, 418, 1035
Wampfler, S. F., Jørgensen, J. K., Bizzarro, M., & Bisschop, S. E. 2014, A&A, 572, A24
Wirström, E. S., Charnley, S. B., Cordiner, M. A., & Milam, S. N. 2012, ApJ, 757, L11
Zeng, S., Jimenez-Serra, I., Cosentino, G., et al. 2017, A&A, 603, A22

Appendix A: Fit results

In this appendix we show the results of the fitting procedure for the $HN^{13}C(1–0)$, $H^{15}NC(1–0)$, $HC^{15}N(1–0)$, DNC(2–1), and $H^{13}CN(1–0)$ lines of all sources (see Sects. 3.1 and 3.2).

Table A.1. Values obtained with a Gaussian fit to the $HN^{13}C$ and $H^{15}NC(1–0)$ lines.

Source	$HN^{13}C(1–0)$				$H^{15}NC(1–0)$			
	v_{LSR} (km s^{-1})	$\Delta v_{1/2}$ (km s^{-1})	$\int T_{MB}\,dv$ (K km s^{-1})	σ (mK)	v_{LSR} (km s^{-1})	$\Delta v_{1/2}$ (km s^{-1})	$\int T_{MB}\,dv$ (K km s^{-1})	σ (mK)
HMSC								
I00117-MM2	−35.27 ± 0.06	2.30 ± 0.02	0.30 ± 0.02	10	−35.1 ± 0.1	1.3 ± 0.4	0.05 ± 0.01	9
AFGL5142-EC	−1.92 ± 0.03	2.47 ± 0.08	1.43 ± 0.04	30	−1.60 ± 0.08	1.9 ± 0.2	0.28 ± 0.03	20
05358-mm3	−15.39 ± 0.02	2.32 ± 0.06	1.65 ± 0.03	20	−14.92 ± 0.08	2.2 ± 0.2	0.32 ± 0.02	20
G034-G2(MM2)	42.24 ± 0.03	1.84 ± 0.08	0.67 ± 0.02	20	42.9 ± 0.2	2.4 ± 0.6	0.1 ± 0.02	10
G034-F1(MM8)	58.74 ± 0.06	1.40 ± 0.09	0.72 ± 0.07	10	59.20 ± 0.09	1.4 ± 0.2	0.07 ± 0.01	10
G034-F2(MM7)	56.93 ± 0.03	1.35 ± 0.06	0.36 ± 0.01	10	57.3 ± 0.1	0.7 ± 0.2	0.02 ± 0.008	7
G028-C1(MM9)	81.19 ± 0.09	1.9 ± 0.1	0.95 ± 0.1	10	80.9 ± 0.1	2.7 ± 0.3	0.15 ± 0.01	9
G028-C3(MM11)	81.56 ± 0.03	1.55 ± 0.08	0.36 ± 0.01	10	82.1 ± 0.2	1.6 ± 0.3	0.05 ± 0.009	8
I20293-WC	7.76 ± 0.09	1.6 ± 0.1	0.58 ± 0.08	10	8.4 ± 0.1	1.2 ± 0.2	0.09 ± 0.01	10
I22134-G	−17.85 ± 0.01	1.47 ± 0.04	0.60 ± 0.01	10	−17.55 ± 0.06	1.5 ± 0.2	0.11 ± 0.01	10
I22134-B	−17.98 ± 0.04	1.5 ± 0.1	0.20 ± 0.01	10	−17.43 ± 0.09	1.0 ± 0.2	0.03 ± 0.006	7
HMPO								
I00117-MM1	−35.44 ± 0.04	1.56 ± 0.09	0.29 ± 0.01	10	−35.1 ± 0.1	1.2 ± 0.2	0.05 ± 0.008	9
AFGL5142-MM	−2.01 ± 0.02	2.68 ± 0.05	1.72 ± 0.03	20	−1.70 ± 0.07	2.2 ± 0.1	0.30 ± 0.02	10
05358-mm1	−15.53 ± 0.02	2.41 ± 0.05	1.73 ± 0.03	20	−15.23 ± 0.06	2.0 ± 0.1	0.28 ± 0.02	10
18089–1732	32.30 ± 0.03	1.6 ± 0.1	0.9 ± 0.2	20	32.7 ± 0.2	1.4 ± 0.3	0.11 ± 0.05	10
18517+0437	44.52 ± 0.02	2.66 ± 0.04	1.54 ± 0.02	10	44.84 ± 0.08	2.5 ± 0.2	0.23 ± 0.01	10
G75-core	0.57 ± 0.07	4.6 ± 0.3	0.86 ± 0.04	10	1.1 ± 0.1	1.9 ± 0.4	0.10 ± 0.01	10
I20293-MM1	6.67 ± 0.01	1.95 ± 0.03	1.49 ± 0.02	10	7.02 ± 0.06	1.8 ± 0.1	0.20 ± 0.01	10
I21307	−45.8 ± 0.01	2.6 ± 0.3	0.20 ± 0.02	10	–	–	–	8
I23385	−49.5 ± 0.1	2.0 ± 0.2	0.27 ± 0.03	10	−49.1 ± 0.2	1.4 ± 0.5	0.04 ± 0.009	9
UC H_{II}								
G5.89-0.39	9.05 ± 0.01	2.87 ± 0.02	9.54 ± 0.07	30	9.35 ± 0.03	2.93 ± 0.08	1.26 ± 0.03	10
I19035-VLA1	33.33 ± 0.05	4.0 ± 0.1	1.01 ± 0.03	20	33.1 ± 0.2	2.6 ± 0.8	0.1 ± 0.02	10
19410+2336	23.16 ± 0.01	1.81 ± 0.03	1.60 ± 0.02	20	23.50 ± 0.03	1.45 ± 0.09	0.22 ± 0.01	10
ON1	12.25 ± 0.01	3.73 ± 0.03	2.89 ± 0.02	10	12.70 ± 0.06	3.3 ± 0.2	0.38 ± 0.02	10
I22134-VLA1	−17.83 ± 0.02	1.45 ± 0.06	0.45 ± 0.01	10	−17.48 ± 0.08	1.5 ± 0.2	0.08 ± 0.009	8
23033+5951	−52.54 ± 0.02	2.15 ± 0.05	0.14 ± 0.02	20	−52.27 ± 0.09	2.2 ± 0.2	0.22 ± 0.02	10
NGC 7538-IRS9	−56.37 ± 0.03	2.21 ± 0.08	0.97 ± 0.03	20	−56.1 ± 0.1	3.0 ± 0.5	0.22 ± 0.02	10

Notes. The errors come from the fitting procedure and do not take the calibration error on T_{MB} into account. In the second and third columns we list the centroid velocities and the FWHM. The fourth column lists the integrated intensities, and the fifth column the rms of the spectra. The cases in which the line is not detected, and therefore only column density upper limits could be obtained as explained in Sect. 3.1, are indicated with a minus. The source names are taken from Fontani et al. (2015b).

Table A.2. Values obtained with Gaussian fits to the $HC^{15}N$ and DNC(2–1) lines.

Source	$HC^{15}N(1–0)$				DNC(2–1)			
	v_{LSR} (km s^{-1})	$\Delta v_{1/2}$ (km s^{-1})	$\int T_{MB}\,dv$ (K km s^{-1})	σ (mK)	v_{LSR} (km s^{-1})	$\Delta v_{1/2}$ (km s^{-1})	$\int T_{MB}\,dv$ (K km s^{-1})	σ (mK)
HMSC								
I00117-MM2	−35.8 ± 0.2	2.2 ± 0.4	0.11 ± 0.02	10	−34.83 ± 0.03	1.73 ± 0.09	0.41 ± 0.02	20
AFGL5142-EC	−2.64 ± 0.07	3.0 ± 0.2	1.07 ± 0.05	30	−1.67 ± 0.03	1.55 ± 0.07	1.50 ± 0.05	60
05358-mm3	−16.01 ± 0.06	2.7 ± 0.1	0.76 ± 0.03	20	−15.38 ± 0.03	2.22 ± 0.08	1.88 ± 0.05	50
G034-G2(MM2)	–	–	–	10	42.18 ± 0.02	1.18 ± 0.06	0.46 ± 0.02	20
G034-F1(MM8)	58.0 ± 0.2	1.4 ± 0.3	0.06 ± 0.01	10	58.5 ± 0.2	1.2 ± 0.2	0.27 ± 0.01	20
G034-F2(MM7)	–	–	–	10	56.74 ± 0.03	0.81 ± 0.07	0.15 ± 0.01	20
*G028-C1(MM9)	80.3 ± 0.4	4 ± 1	0.14 ± 0.03	10	81.4 ± 0.1	1.6 ± 0.2	0.29 ± 0.04	20
G028-C3(MM11)	–	–	–	10	81.32 ± 0.09	1.2 ± 0.2	0.1 ± 0.01	20
I20293-WC	7.5 ± 0.1	1.3 ± 0.2	0.13 ± 0.04	10	7.80 ± 0.01	1.26 ± 0.02	0.91 ± 0.03	20
I22134-G	−18.46 ± 0.03	1.56 ± 0.07	0.39 ± 0.01	10	−18.13 ± 0.02	1.17 ± 0.06	0.34 ± 0.02	20
I22134-B	−18.25 ± 0.08	1.3 ± 0.2	0.07 ± 0.008	9	−18.37 ± 0.04	1.03 ± 0.07	0.12 ± 0.08	10
HMPO								
I00117-MM1	−36.0 ± 0.1	2.1 ± 0.2	0.15 ± 0.06	10	−35.48 ± 0.05	1.8 ± 0.1	0.26 ± 0.02	20
AFGL5142-MM	−2.67 ± 0.04	3.3 ± 0.1	1.42 ± 0.04	20	−1.62 ± 0.04	3.2 ± 0.1	2.55 ± 0.08	60
05358-mm1	−16.12 ± 0.05	2.8 ± 0.1	0.80 ± 0.03	20	−15.62 ± 0.03	2.11 ± 0.07	1.50 ± 0.04	40
18089–1732	32.15 ± 0.07	2.8 ± 0.2	0.820 ± 0.002	20	32.19 ± 0.05	1.9 ± 0.1	0.74 ± 0.04	30
18517+0437	44.00 ± 0.04	2.9 ± 0.1	0.89 ± 0.03	20	44.37 ± 0.04	2.77 ± 0.09	1.48 ± 0.04	40
G75-core	0.07 ± 0.01	3.1 ± 0.2	0.79 ± 0.09	10	0.3 ± 0.2	2.5 ± 0.2	0.28 ± 0.01	20
I20293-MM1	6.42 ± 0.05	2.2 ± 0.1	0.44 ± 0.02	20	6.53 ± 0.06	2.6 ± 0.2	0.76 ± 0.04	30
I21307	−46.2 ± 0.1	2.2 ± 0.2	0.13 ± 0.01	10	−46.29 ± 0.08	1.7 ± 0.2	0.18 ± 0.02	20
I23385	−50.1 ± 0.01	2.4 ± 0.3	0.32 ± 0.03	10	−49.43 ± 0.07	1.2 ± 0.2	0.15 ± 0.02	20
UC H_{II}								
G5.89-0.39	8.94 ± 0.03	3.9 ± 0.1	4.4 ± 0.2	20	8.06 ± 0.01	1.98 ± 0.04	2.28 ± 0.06	30
I19035-VLA1	32.9 ± 0.2	4.7 ± 0.4	0.35 ± 0.03	10	32.9 ± 0.1	2.6 ± 0.3	0.34 ± 0.05	20
19410+2336	22.60 ± 0.03	1.94 ± 0.08	0.66 ± 0.02	20	22.87 ± 0.01	1.85 ± 0.04	1.31 ± 0.02	20
ON1	11.83 ± 0.05	4.1 ± 0.1	1.01 ± 0.03	10	12.59 ± 0.04	5.11 ± 0.09	1.69 ± 0.03	20
I22134-VLA1	−18.34 ± 0.03	1.47 ± 0.08	0.09 ± 0.001	10	−18.19 ± 0.04	1.72 ± 0.08	0.33 ± 0.01	20
23033+5951	−52.93 ± 0.06	2.6 ± 0.1	0.51 ± 0.02	20	−52.48 ± 0.02	1.11 ± 0.06	0.64 ± 0.004	30
NGC 7538-IRS9	−56.82 ± 0.08	4.1 ± 0.3	0.77 ± 0.04	20	−56.54 ± 0.05	1.9 ± 0.1	0.61 ± 0.03	30

Notes. The errors come from the fitting procedure and do not take the calibration error on T_{MB} into account. In the second and in the third colums we list the centroid velocities and the line FWHM, respectively. The fourth column lists the integrated intensities, and the fifth column the rms of the spectra. The cases in which the line is not detected, and therefore only column density upper limits could be obtained as explained in Sect. 3.1, are indicated with a minus. * Tentative detection, as explained in Sect. 3.1.

Table A.3. Values obtained from the hyperfine fit of the $H^{13}CN(1–0)$ lines.

Source	v_{LSR} (km s^{-1})	$\Delta v_{1/2}$ (km s^{-1})	τ	$T_A \times \tau$ (K)	σ (mK)	$\int T_{MB}\, dv$ (K km s^{-1})
			HMSC			
I00117-MM2	−36.37 ± 0.05	1.8 ± 0.1	0.1 ± 0.1	0.142 ± 0.008	10	0.42 ± 0.02
AFGL5142-EC	−3.35 ± 0.02	3.30 ± 0.04	0.10 ± 0.06	0.94 ± 0.01	30	5.81 ± 0.08
05358-mm3	−16.65 ± 0.03	3.00 ± 0.05	0.10 ± 0.04	0.80 ± 0.01	30	4.51 ± 0.07
G034-G2(MM2)	41.1 ± 0.1	1.7 ± 0.2	0.1 ± 0.4	0.087 ± 0.007	10	0.23 ± 0.02
G034-F1(MM8)	57.62 ± 0.08	1.7 ± 0.1	0.1 ± 0.4	0.16 ± 0.01	10	0.50 ± 0.02
G034-F2(MM7)	55.69 ± 0.04	0.8 ± 0.1	0.25 ± 0.02	0.11 ± 0.01	10	0.23 ± 0.01
G028-C1(MM9)	79.43 ± 0.05	3.09 ± 0.09	0.1 ± 0.2	0.180 ± 0.006	10	1.02 ± 0.03
G028-C3(MM11)	80.31 ± 0.08	2.2 ± 0.3	0.5 ± 0.7	0.12 ± 0.03	10	0.45 ± 0.03
I20293-WC	6.83 ± 0.06	1.0 ± 0.1	0.60 ± 0.03	0.15 ± 0.02	10	1.33 ± 0.03
I22134-G	−19.04 ± 0.01	1.65 ± 0.03	0.10 ± 0.03	0.63 ± 0.01	10	1.85 ± 0.03
I22134-B	−18.95 ± 0.02	1.43 ± 0.06	0.1 ± 0.4	0.164 ± 0.006	10	0.45 ± 0.02
			HMPO			
I00117-MM1	−36.54 ± 0.03	1.96 ± 0.09	0.3 ± 0.3	0.21 ± 0.02	10	0.74 ± 0.02
AFGL5142-MM	−3.43 ± 0.01	3.27 ± 0.03	0.26 ± 0.06	1.27 ± 0.03	20	7.52 ± 0.05
05358-mm1	−16.8 ± 0.02	2.99 ± 0.04	0.50 ± 0.02	0.91 ± 0.01	20	4.68 ± 0.06
18089–1732	31.8 ± 0.4	2 ± 1	0.1 ± 0.1	01.48 ± 0.02	30	6.51 ± 0.05
18517+0437	43.29 ± 0.01	2.97 ± 0.02	0.1 ± 0.03	1.024 ± 0.007	20	5.76 ± 0.05
G75-core	−0.596 ± 0.004	2.5 ± 0.1	0.1 ± 0.02	0.48 ± 0.02	10	3.27 ± 0.02
I20293-MM1	5.79 ± 0.02	2.38 ± 0.03	0.100 ± 0.002	0.80 ± 0.01	20	3.64 ± 0.04
I21307	−47.00 ± 0.04	2.3 ± 0.1	0.2 ± 0.3	0.18 ± 0.02	10	0.75 ± 0.03
I23385	−50.9 ± 0.3	1 ± 1	0.6 ± 0.1	0.26 ± 0.01	10	1.16 ± 0.02
			UC H_{II}			
G5.89-0.39	8.24 ± 0.01	3.83 ± 0.01	0.12 ± 0.01	3.75 ± 0.2	30	20.97 ± 0.05
I19035-VLA1	32.17 ± 0.05	4.4 ± 0.1	0.4 ± 0.2	0.30 ± 0.02	10	2.26 ± 0.04
19410+2336	22.01 ± 0.002	2.186 ± 0.002	0.10 ± 0.02	1.090 ± 0.005	20	4.64 ± 0.04
ON1	11.12 ± 0.02	3.71 ± 0.04	0.73 ± 0.08	0.93 ± 0.03	10	5.55 ± 0.04
I22134-VLA1	−18.98 ± 0.01	1.76 ± 0.03	0.10 ± 0.03	0.513 ± 0.007	10	1.67 ± 0.03
23033+5951	−53.63 ± 0.02	2.73 ± 0.02	0.10 ± 0.02	0.621 ± 0.003	20	3.17 ± 0.04
NGC 7538-IRS9	−57.64 ± 0.02	3.60 ± 0.04	0.10 ± 0.03	0.65 ± 0.01	20	4.43 ± 0.04

Notes. The errors come from the fitting procedure and do not take the calibration error on T_{MB} into account. The second and third colums list the centroid velocities and the FWHM, respectively. The fourth and fifth columns list the optical depths and the antenna temperatures times the optical depths. The sixth column lists the rms of the spectra, and the last column shows the integrated intensities that in this case are not obtained from the fitting procedure, but from the PRINT AREA command in CLASS.

Appendix B: Spectra

In this appendix we show all spectra of the $HN^{13}C(1–0)$, $H^{13}CN(1–0)$, $H^{15}NC(1–0)$, $HC^{15}NC(1–0)$, and DNC(2–1) transitions for all the sources.

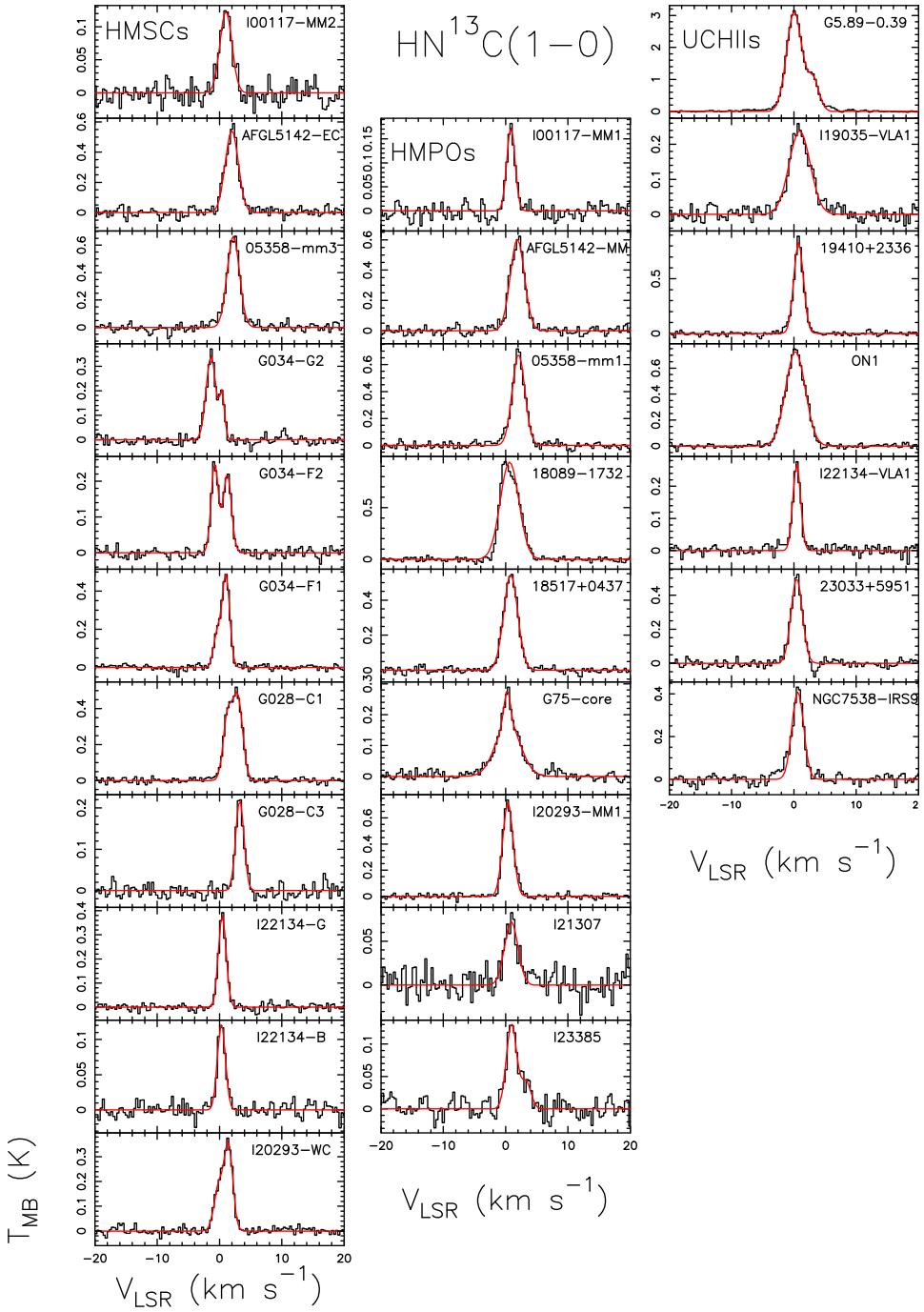

Fig. B.1. Spectra of $HN^{13}C(1–0)$ obtained for the sources classified as HMSCs (*first column*), HMPOs (*second column*), and UC HII regions (*third column*). For each spectrum the *x*-axis represents a velocity interval of ±20 km s^{-1} around the systemic velocity listed in Table 1 of Fontani et al. (2015b). The *y*-axis shows the intensity in main-beam temperature units. The red curves are the best Gaussian fits obtained with CLASS. For some sources (I20293-WC, G034-G2, G034-F2, G5.89-0.39, G034-F1, G028-C1, and I23385), we have observed two components: we have fitted both lines and used only the line centered on the systemic velocity of the source to compute the column densities.

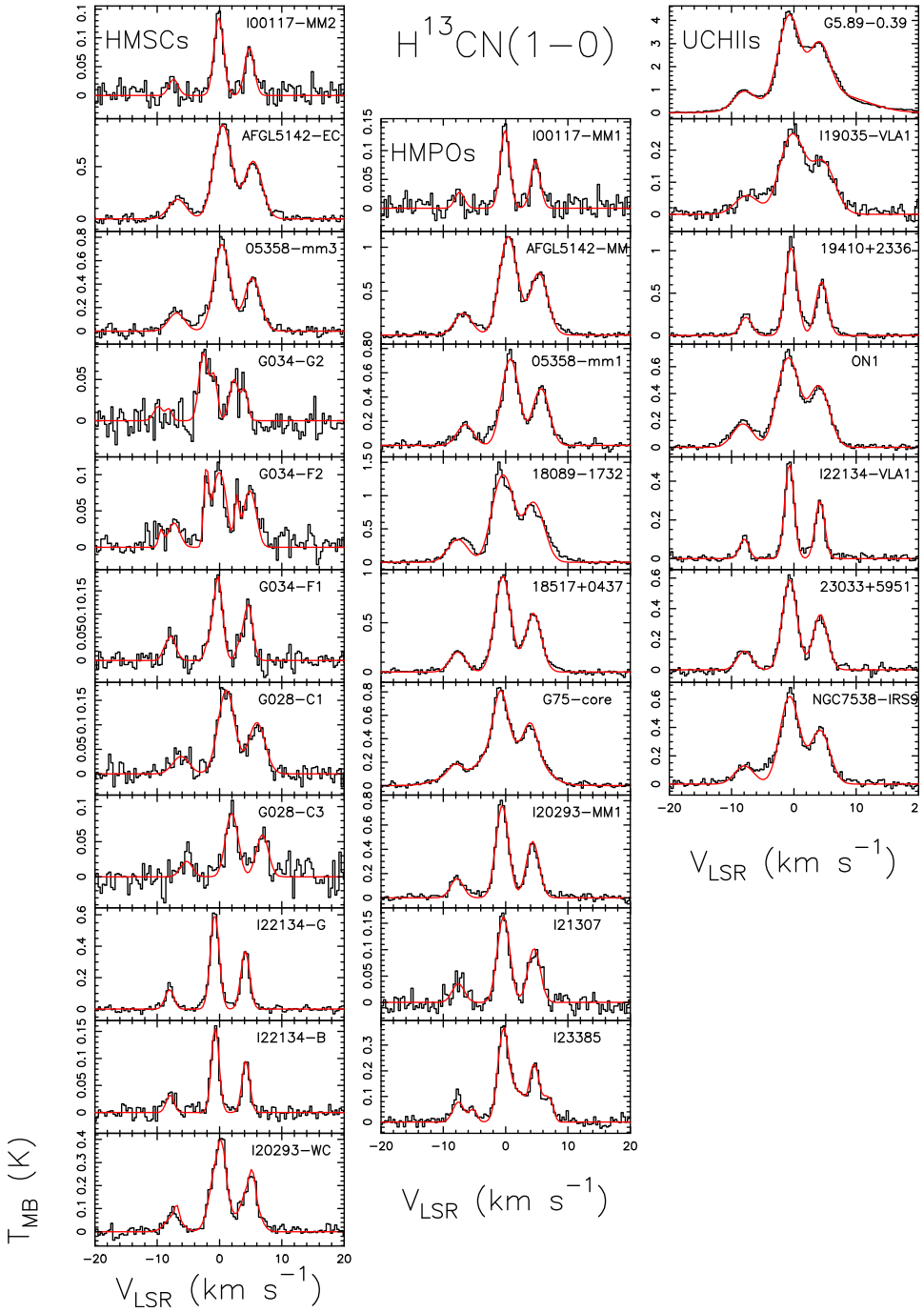

Fig. B.2. Same as Fig. A.3 for $H^{13}CN(1–0)$. Here the red curves are the best hyperfine fits obtained with CLASS. We note the presence of the second velocity component in the same sources that were indicated in the caption of Fig. B.1.

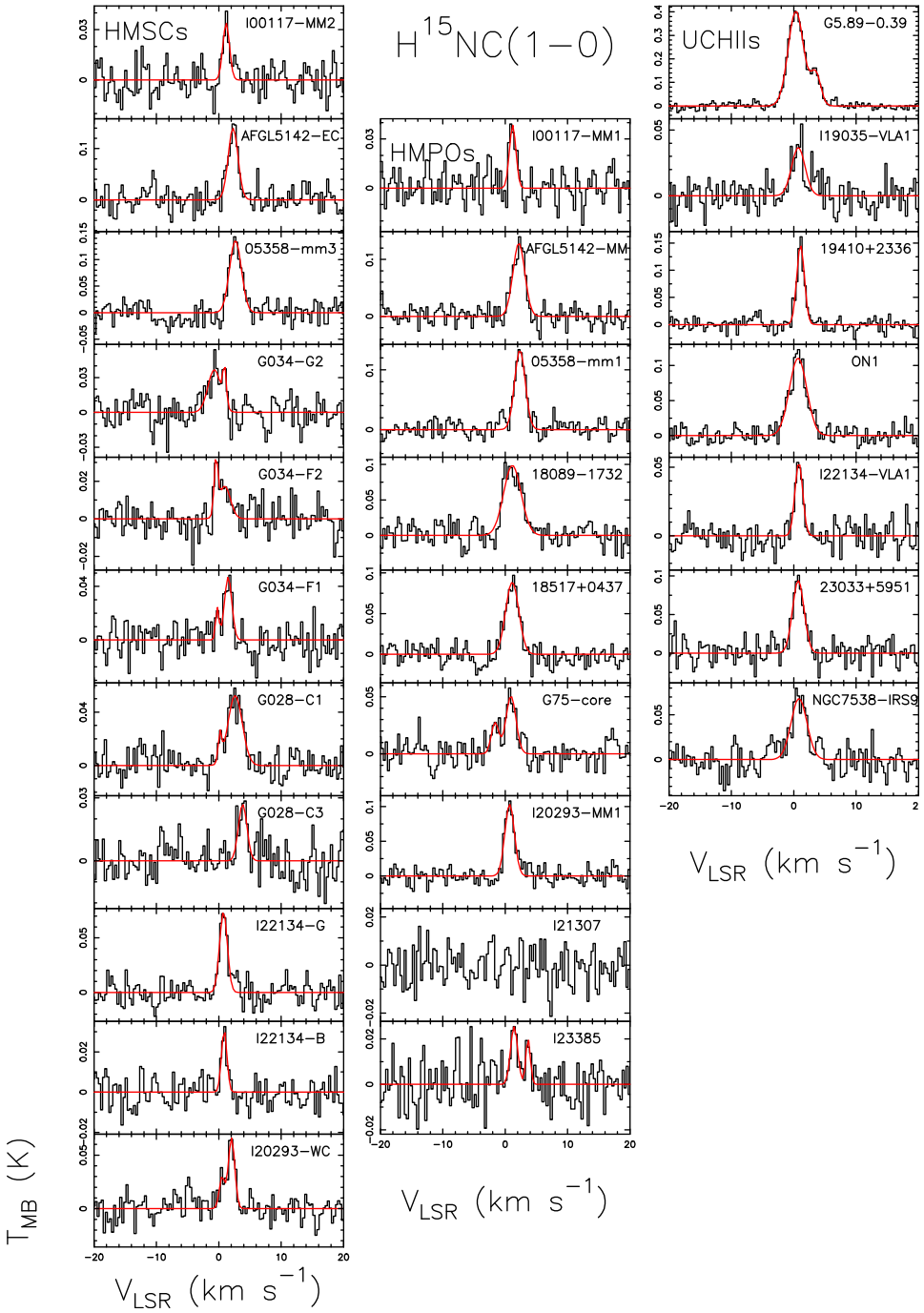

Fig. B.3. Same as Fig. A.3 for $H^{15}NC(1–0)$. For I21307, this line was not detected, and we have obtained a column density upper limit, as explained in Sect. 3.1.

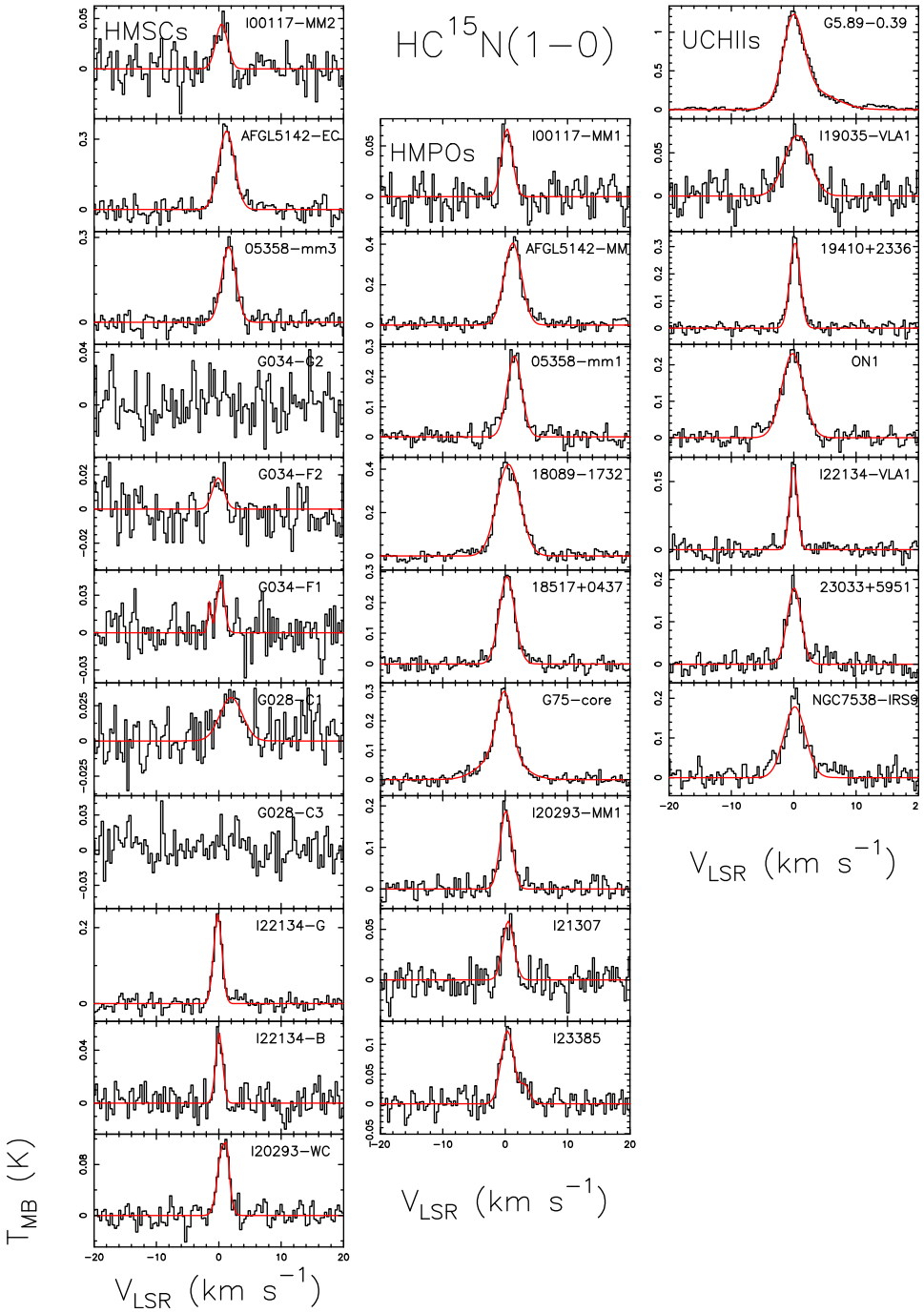

Fig. B.4. Same as Fig. A.3 for HC^{15}N(1–0). For G034-G2, G028-C3, and G034-F2, the line was not detected, and we obtained a column density upper limit, as explained in Sect. 3.1. For G034-F1 we did not have a clear detection, but we have obtained from the Gaussian fit that $T_{\rm MB}^{\rm peak} \gtrsim 2.5\sigma$, we have computed as usual the column density, and we refer to this latter as "tentative detection" (see also Table A.2).

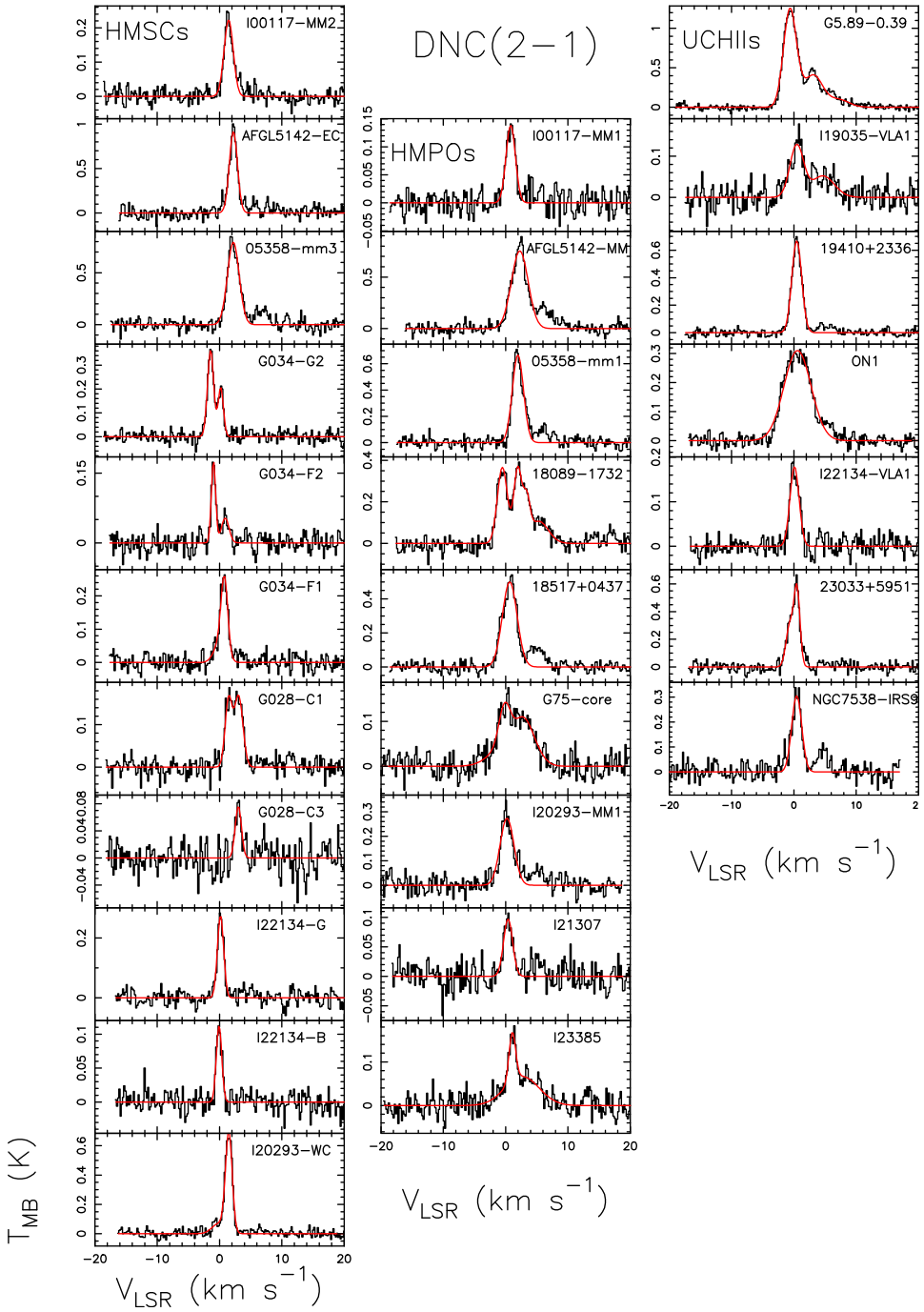

Fig. B.5. Same as Fig. A.3 for DNC(2–1). For evolved sources (HMPOs and UC HII) the acetaldehyde line is also present, as explained in Sect. 3.2: when possible, we have excluded the line from the Gaussian fit, otherwise we have fitted the two lines together and used only the DNC(2–1) to compute the column densities.

Appendix C: Comparison with other molecules

In this appendix, we compare the $^{14}N/^{15}N$ ratios obtained in this paper and in Fontani et al. (2015a) for all the common sources. The $^{12}C/^{13}C$ we used and the Galactocentric distances are also listed.

Table C.1. Comparison between $^{14}N/^{15}N$ ratios obtained from HNC and HCN in this work and those obtained from N_2H^+ and CN by Fontani et al. (2015a).

Source	$\frac{HNC}{H^{15}NC}$	$\frac{HCN}{HC^{15}N}$	$\frac{N_2H^+}{^{15}NNH^+}$	$\frac{N_2H^+}{N^{15}NH^+}$	$\frac{CN}{C^{15}N}$	$\frac{^{12}C}{^{13}C}$	D_{GC} (kpc)
			HMSC				
I00117-MM2	460 ± 80	282 ± 54	670 ± 98	≥561	–	69	9.5
AFGL5142-EC	398 ± 39	398 ± 18	1100 ± 360	≥1034	330 ± 67	74	10.3
05358-mm3	388 ± 28	433 ± 20	210 ± 12	180 ± 13	400 ± 90	74	10.3
G034-G2(MM2)	365 ± 71	≥147	≥856	≥873	–	50	6.3
G034-F1(MM8)	495 ± 72	369 ± 80	≥566	≥672	–	47	5.8
G034-F2(MM7)	783 ± 263	≥168	≥195	≥232	–	47	5.8
G028-C1(MM9)	260 ± 30	287 ± 55	≥1217	≥1445	–	40	4.7
G028-C3(MM11)	338 ± 53	≥250	–	–	–	40	4.7
I20293-WC	439 ± 90	620 ± 180	65 ± 69	550 ± 98	–	62	8.3
I22134-G	369 ± 35	322 ± 14	≥232	≥197	330 ± 150	69	9.5
I22134-B	414 ± 85	406 ± 50	≥316	≥322	–	69	9.5
			HMPO				
I00117-MM1	388 ± 75	345 ± 38	220 ± 60	≥233	≥250	69	9.5
AFGL5142-MM	433 ± 27	387 ± 10	740 ± 97	1300 ± 210	190 ± 23	74	10.3
05358-mm1	466 ± 29	432 ± 18	190 ± 20	180 ± 23	240 ± 40	74	10.3
18089–1732	385 ± 204	338 ± 9	1000 ± 400	800 ± 100	450 ± 100	43	5
18517+0437	349 ± 22	326 ± 9	390 ± 53	260 ± 20	310 ± 80	51	6.4
G75-core	554 ± 84	258 ± 3	≥209	≥240	240 ± 50	63	8.4
I20293-MM1	481 ± 33	504 ± 25	790 ± 67	370 ± 42	–	62	8.3
I21307	≥317	389 ± 46	≥301	≥346	≥175	68	9.3
I23385	639 ± 189	290 ± 26	≥81	≥66	–	81	11.4
			UC HII				
G5.89-0.39	432 ± 10	255 ± 12	320 ± 25	450 ± 51	350 ± 160	55	7.2
I19035-VLA1	570 ± 107	340 ± 27	≥572	≥754	≥270	54	7
19410+2336	431 ± 24	405 ± 12	450 ± 96	500 ± 100	430 ± 250	58	7.7
ON1	467 ± 19	327 ± 8	460 ± 22	350 ± 33	350 ± 220	60	8
I22134-VLA1	364 ± 43	390 ± 18	≥80	≥108	250 ± 84	69	9.5
23033+5951	397 ± 35	458 ± 21	900 ± 400	700 ± 250	≥370	74	10.2
NGC 7538-IRS9	331 ± 37	410 ± 20	≥255	≥294	230 ± 90	72	9.9

Notes. Columns 2 and 3 list the $^{14}N/^{15}N$ ratios for HNC and HCN found in this work. Columns 4–6 list the $^{14}N/^{15}N$ ratios for N_2H^+ and CN found by Fontani et al. (2015a). Column 7 lists the values of $^{12}C/^{13}C$ found from the gradient with the Galactocentric distances given by Milam et al. (2005). The last column lists the Galactocentric distances of the sources obtained from the source distance from the Sun (taken from Fontani et al. 2011) and the corresponding Galactic longitude.